Essential requirement for Jupiter Microtubule Associated Homolog 2 in NAADP-evoked Ca^{2+} signaling

Gihan S. Gunaratne[1,2], Eugen Brailoiu[3], Shijun He[4], Ellen M. Unterwald[3], Sandip Patel[5]
James T. Slama[3]†, Timothy F. Walseth[1]† and Jonathan S. Marchant[2]†*

[1]Department of Pharmacology, University of Minnesota Medical School, 312 Church St., Minneapolis, MN 55455

[2]Department of Cell Biology, Neurobiology & Anatomy, Medical College of Wisconsin, 8701 Watertown Plank Road, Milwaukee, WI 53226

[3]Center for Substance Abuse Research, Lewis Katz School of Medicine at Temple University, Philadelphia, PA 19140

[4]Department of Medicinal & Biological Chemistry, University of Toledo College of Pharmacy and Pharmaceutical Sciences, 3000 Arlington Avenue, Toledo, OH 43614

[5]Department of Cell and Developmental Biology, University College London, Gower Street, London WC1E 6BT, UK

† Co-Senior Authorship
* Correspondening Author: Email: JMarchant@mcw.edu

Figures: 7x Figures, 1x Table; Supplementary Materials: 2x Supplementary Figures

Short Title: JPT2 as a mediator of NAADP action

Keywords: Ca^{2+} release, ion channel, two pore channels, photolabeling, coronavirus

One sentence summary: JPT2 is identified as a novel protein in the two-pore channel (TPC) complex required for TPC-dependent Ca^{2+} signaling and coronaviral entry

Abstract

Nicotinic acid adenine dinucleotide phosphate (NAADP) is a second messenger that releases Ca^{2+} from acidic organelles through activation of two pore channels (TPCs) to regulate endo-lysosomal trafficking events. NAADP action is mediated by NAADP-binding protein(s) that confer NAADP-sensitivity to TPCs but their molecular identity is unknown. Here we use a novel 'clickable' NAADP-based photoprobe to isolate human NAADP-binding proteins and identify Jupiter Microtubule Associated Homolog 2 (JPT2) as a TPC accessory protein required for endogenous NAADP-evoked Ca^{2+} signaling. JPT2 was also required for translocation of a severe acute respiratory syndrome coronavirus 2 (SARS-CoV-2) pseudovirus through the endolysosomal system. JPT2 is thus identified as a novel component of the NAADP receptor complex essential for TPC-dependent Ca^{2+} signaling and control of coronaviral entry.

Introduction

The second messenger nicotinic acid adenine dinucleotide phosphate (NAADP) releases Ca^{2+} from acidic Ca^{2+} stores within the endolysosomal system (*1, 2*). NAADP-evoked Ca^{2+} release regulates numerous cellular processes (*2, 3*), including the trafficking of physiological substrates and pathological cargoes (for example, viruses (*4-7*)) through the endolysosomal system. Dysfunction of this pathway has been implicated in several disease states (*8*).

Despite the (patho)physiological importance of NAADP-evoked Ca^{2+} signaling, our understanding of the molecular basis for NAADP action remains incomplete. Several ion channel targets for NAADP have been proposed, with the majority of evidence supporting NAADP activation of two-pore channels (TPCs) resident in endosomes and lysosomes (*9, 10*). However, no direct binding site for NAADP has been identified on TPCs in over a decade since their first characterization in mammals (*11-13*) Rather, NAADP is thought to exert its potent Ca^{2+}-mobilizing activity by binding to unidentified NAADP-binding accessory protein(s) (NAADP-BPs) within the TPC channel complex (*14*). In T-lymphocytes, NAADP has alternatively been shown to release Ca^{2+} from the endoplasmic reticulum (ER) through the type 1 ryanodine receptor (RyR1, (*15*)). No direct NAADP binding site has been identified on RyR1.

Direct experimental support for the NAADP-BP model, derives from photolabeling studies where NAADP-derivatized photoprobes identify a low molecular weight NAADP-BP (~22/23kDa) distinct from TPCs and RyRs in a variety of mammalian cells (*9, 16-20*). The binding characteristics of NAADP to the NAADP-BP recapitulated key properties of NAADP-evoked Ca^{2+}

release, including a characteristic pharmacology, high affinity and selectivity for NAADP over NADP (~11-fold, (*16*)). Photolabeling of the NAADP-BP, but not NAADP-evoked Ca^{2+} release, persists in TPC knockout models (*9, 16*) and NAADP-BPs are co-immunoprecipitated with TPCs in sea urchin egg homogenates (*17*). Therefore, the ~23kDa NAADP-BP is a distinct molecular entity from TPCs, the identity of which is unknown. Here, we utilize a chemical biology and proteomic approach to identify the photolabeled ~23kDa mammalian NAADP-BP as Jupiter microtubule associated homolog 2 (JPT2) and reveal its essential role in both NAADP-evoked Ca^{2+} signaling and cell entry of severe acute respiratory syndrome coronavirus 2 (SARS-CoV-2) pseudovirus.

Results

Photolabeling of JPT2 by a 'clickable' NAADP-derived affinity probe

A novel bifunctional photoprobe, [^{32}P]-alkyne-'all-in-one-click' (AIOC)-NAADP, was synthesized and used to profile NAADP-BPs in a variety of human cell types. In human erythrocytes, analysis of radiolabeling patterns surprisingly revealed enrichment of a ~23kDa NAADP-BP (Fig. 1, A and B) compared to intensities seen in other human cell lines (*16, 18-20*). Photolabeling of the ~23kDa NAADP-BP was protected by co-incubation with NAADP (Fig. 1, A and B).

Characterization of this erythrocyte NAADP-BP was performed in further photolabeling assays. Fractionation of erythrocyte whole-cell lysate revealed the NAADP-BP was exclusively found in the soluble ('S20') supernatant (Fig. 1, C and D). Incubation with other nucleotide analogs, or other Ca^{2+}-mobilizing messengers (10μM), failed to shield photolabeling of the NAADP-BP (Fig. 1, E and F). However, incubation with NAADP, unlabeled alkyne-AIOC-NAADP, or high concentrations of NADP inhibited photolabeling. Characterization of selectivity demonstrated ~11-fold selectivity for NAADP (IC_{50}=80±7nM) over NADP (IC_{50}=871±120nM, Fig. 1, G and H) in agreement with previous photolabeling data (*16*). Together, these data authenticate human erythrocytes as an enriched biological source of the ~23kDa NAADP-BP.

Previous efforts to identify this NAADP-BP from other mammalian cells has proved challenging, owing to low expression of the endogenous NAADP-BP. However, the abundance of the ~23kDa NAADP-BP in erythrocytes provided better opportunity for a purification effort from the gram-quantities of protein available from an easily sourced material (Fig. 2A). Additionally, synthesis

of the bifunctional probe ([^{32}P]-alkyne-AIOC-NAADP, Fig. 2B) with both a photoactivatable azide and a clickable alkynyl moiety permitted coupling of NAADP-BP photolabeling to a subsequent enrichment strategy. This strategy is outlined schematically in Figure 2A, which depicts the series of chromatography steps used to enrich the NAADP-BP from erythrocyte S20 samples. Proteins were sequentially fractionated using a multistep protocol to yield ~200-fold enrichment (fig. S1). In this scheme, a phosphoprotein enrichment resin was employed to concentrate the NAADP-BP using a batch-binding method. When NAADP-BP was not photolabeled it was retained by the phosphoprotein resin, while probe-bound NAADP-BP passed through (fig. S1). This property was exploited to collect unlabeled eluate following an initial fractionation and elution from the phosphoprotein resin. The unlabeled fraction was then photolabeled with a saturating concentration of alkyne-AIOC-NAADP (spiked with a traceable amount of [^{32}P]-alkyne-AIOC-NAADP) to ensure that all NAADP-BP binding sites were occupied. Probe-bound samples were then incubated with fresh phosphoprotein enrichment resin for a second round of fractionation (Fig. 2, C and D). Probe-bound NAADP-BPs were biotinylated using a copper-catalyzed alkyne-azide cycloaddition (CuAAC) using 'click chemistry' and the biotinylated proteins captured using neutravidin. This protocol resulted in the isolation of a ~23kDa protein detectable by both silver stain and phosphorimaging (Fig. 2E).

Gel bands from both input control samples and biotin pulldowns were excised and processed for mass spectrometry. Inspection of total spectra revealed JPT2 as the most highly enriched protein hit (Table 1). Few JPT2 spectra were detected in input control samples, while >70-fold enrichment of JPT2 spectra was detected in CuAAC biotin-pulldown samples. No JPT2 spectra

were detected in non-biotinylated CuAAC control samples. Moreover, nearly complete peptide coverage of JPT2 was detected (186 out of 190 amino acids). As an alternative ranking measure. total spectral counts from protein hits were processed to yield normalized spectral abundance factor (NSAF) values. Hits were ranked after NSAF values for non-biotinylated control samples were subtracted from NSAF values for the CuAAC biotin-azide-Plus pulldown samples, which again ranked JPT2 as the top NAADP-BP candidate (Fig. 2F). Erythrocyte chromatography fractions were then immunoblotted for JPT2 and this confirmed a progressive enrichment of JPT2 during the serial chromatography procedure (Fig. 2G).

JPT2 properties and expression profile

JPT2 is a short, highly basic protein containing four repeated consensus ('PPGGxxSxxF') sequences, with an additional motif ('MASNIF') characteristic of this gene family located between the first two of these repeats (Fig. 3A, (16)). *JPT2* mRNA is broadly expressed in human cell lines but is abundant in human cell lines (SKBR3 (7), U2OS (15)) commonly used to study endogenous NAADP-evoked Ca^{2+} signals (Fig. 3A). In terms of evolutionary pedigree, both members of this conserved gene family (*JPT1* and *JPT2*) are present in numerous vertebrates (*21*). However, only a single *JPT* gene is present in basal chordates, echinoderms and most protostomal phyla (Fig. 3B). Identification of JPT homologues in sea squirts, sea urchins, starfish, and sea slugs is consistent with functional NAADP responses in these organisms (*22-25*). JPTs are notably absent in the round worm (*C. elegans*) similar to the absence of TPCs (Fig. 3B). However, JPT isoforms appear to be absent in platyhelminths despite the presence of TPCs (Fig. 3B). Conversely, a *JPT* gene is present in fruit flies (*Drosophila*) where TPCs are absent (Fig.

3B). *Drosophila* Jupiter (~27% sequence identity with human JPT2) is a microtubule-associated protein (*26*) whereas JPT2 is localized to the cell surface, cytoplasm and nucleus in human cells (*21, 27, 28*).

Knockdown and pulldown of endogenous JPT2

To validate JPT2 as the photolabeled NAADP-BP, we used two independent siRNAs to knockdown endogenous JPT2 in HEK293 and U2OS cells. Lysates from siRNA-treated cells were photolabeled, and the relative intensity of photolabeling patterns assessed. Cells transfected with either of two *JPT2*-specific siRNAs exhibited reduced photolabeling of the endogenous ~23kDa NAADP-BP (decrease of ~60% in HEK293, ~50-65% in U2OS, Fig. 4, A to D). In contrast, transfection of two non-targeting siRNAs did not reduce ~23kDa NAADP-BP photolabeling (Fig. 4, A to D). JPT2 knockdown was verified by Western blotting (fig. S2). Immunoprecipitation studies using two independent antibodies specific to JPT2 were then performed in lysates from erythrocytes (S20) and U2OS cells (S200 lysates, (*20*)). Immunoprecipitates were probed with [^{32}P]-alkyne-AIOC-NAADP. Both antibodies pulled down the 23kDa NAADP-BP (Fig. 4, E to H). In contrast, eluates from immunoprecipitations using isotyped control IgG antibody displayed no photolabeling. Therefore, both knockdown and immunoprecipitation of endogenous JPT2 validated its identity as the ~23kDa protein labelled by the NAADP-derived photoprobe.

Recombinant JPT2 selectively binds NAADP

To interrogate whether JPT2 acts a NAADP-binding protein using an orthogonal approach, we performed [^{32}P]-NAADP binding experiments to recombinant human JPT2 isolated from *E. coli*.

Recombinant JPT2 was incubated with [^{32}P]-NAADP in the presence of increasing NAADP or NADP concentrations and binding determined after filtration (Fig. 5A). Densitometry revealed JPT2 selectively bound NAADP, with displacement of bound [^{32}P]-NAADP being ~17-fold more potent with NAADP (IC_{50}=20±3.6nM) than with NADP (IC_{50} = 334±76nM, Fig. 5B).

JPT2 is a TPC1 accessory protein that regulates responsiveness to NAADP

Does JPT2 interact with TPCs to regulate NAADP-sensitive Ca^{2+} release? First, to assess TPC interactivity, reciprocal immunoprecipitations were performed. In HEK293 cells, overexpressing epitope-tagged TPC constructs (TPC1-GFP, TPC2-GFP), pull-down of endogenous JPT2 resulted in co-immunoprecipitation of TPC1-GFP but not TPC2-GFP (Fig. 6A). Reciprocally, pull-down of GFP-tagged TPC1, but not TPC2, resulted in co-immunoprecipitation of endogenous JPT2. Second, to assess the impact of JPT2 on endogenous NAADP-evoked Ca^{2+} signals, Ca^{2+} imaging experiments were performed in single cells directly microinjected with NAADP. In U2OS cells, microinjection of NAADP, but not buffer alone, evoked a rapid Ca^{2+} transient, as shown previously (*20*). This NAADP-evoked Ca^{2+} signal was similar in cells treated with two unique control siRNAs (Fig. 6, B and C). However, in cells treated with either of the dual siRNAs targeting endogenous JPT2, the amplitude of Ca^{2+} signals caused by NAADP microinjection was strongly inhibited (Fig. 6, B and C). The size of NAADP responses in cells treated with siRNA targeting JPT2 was not statistically different from signals evoked by buffer injection (Fig. 6C).

JPT2 regulates coronavirus entry

NAADP-evoked Ca^{2+} release is important for controlling the trafficking of pathogens within the endolysosomal system that are internalized as part of their infective cycle (*4-6, 29, 30*). For example, we have demonstrated that TPCs regulate endolysosomal translocation of a Middle East Respiratory Syndrome pseudovirus (MERS-CoV, (*5, 30*)). Is JPT2, as an essential component of NAADP-evoked Ca^{2+} responsiveness (Fig. 6, B and C), also required for CoV infectivity? To investigate this issue, we analyzed the role of JPT2 and the TPC complex in the translocation of a SARS-CoV-2 pseudovirus. Viral translocation trafficking was monitored using a reporter assay (*5, 30, 31*) where the pseudovirus generates a luminescence signal after release into the cytoplasm, thereby reporting the efficiency of subcellular translocation events (ACE2 receptor binding, internalization, endolysosomal processing and transit, cytoplasmic release). First, we tested the effect of the Ca^{2+} chelating agent BAPTA-AM, which resulted in nearly complete inhibition of SARS-CoV-2 pseudovirus infectivity, indicating that intracellular Ca^{2+} signaling plays an essential role for SARS-CoV-2 cellular entry. Next, we analyzed the effects of previously screened inhibitors of NAADP-evoked Ca^{2+} release. Tetrandrine, a TPC blocker (*4*), effective against replication-competent SARS-CoV-2 (*32*), caused a marked inhibition of SARS-CoV-2 pseudovirus translocation (Fig. 7A). Four other anti-MERS-CoV compounds that have been shown to act as inhibitors of NAADP-evoked Ca^{2+} release (PF-543, SKF96365, racecadotril and salmeterol (*30*)) also inhibited cell entry of the SARS-CoV-2 pseudovirus (Fig. 7A). However, drugs targeting IP_3Rs (2-APB, xestospongin) or RyRs (ryanodine) had no effect.

Loss of function analyses were then performed using siRNAs targeting either JPT1, JPT2, TPCs, or the endolysosomal ion channel TRPML1 (Fig. 7B). Whereas independent control siRNAs, or

dual siRNAs targeting JPT1 or TRPML1, failed to inhibit SARS-CoV-2 pseudovirus translocation, knockdown of endogenous JPT2 markedly inhibited SARS-CoV-2 infectivity, decreasing luminescence to values comparable seen with siRNAs targeting TPCs (Fig. 7B). Inhibition of SARS-CoV-2 was specific to pseudoviral translocation through the acidic Ca^{2+} stores (mediated by spike protein engagement of ACE2), as overexpression of the membrane-anchored protease TMPRSS2 (to cleave the S protein into a fusogenic state at the cell surface) circumvented the observed inhibition (Fig. 7, C and D).

Collectively, these data show that JPT2 is both a NAADP-BP (Fig. 5) and TPC accessory protein (Fig. 6A). JPT2 function is essential for conferring NAADP sensitivity in human cells, as shown by its role in NAADP-evoked Ca^{2+} signaling (Fig. 6B) and SARS-CoV-2 cell entry, a NAADP-dependent cellular process (Fig. 7).

Discussion

Two advances facilitated the unmasking of JPT2 as the ~23kDa NAADP-BP previously identified in human cells (*16, 18*). First, the synthesis of a novel bifunctional probe (^{32}P-alkyne-'all-in-one clickable'-NAADP) to selectively photolabel and then enrich NAADP-BPs. Second, the serendipitous discovery that human erythrocytes contain an abundant source of the ~23kDa NAADP-BP. The latter was a surprising finding given the lack of cytoplasmic organelles and intracellular Ca^{2+} stores in mature red blood cells (*33*), although NAADP has been shown to be present (*34*). The erythrocyte NAADP-BP exhibited identical characteristics to the previously characterized mammalian ~23kDa NAADP-BP including a characteristic pharmacology and selectivity for NAADP over NADP (Fig. 1, (*9, 16-20*)). Consistent with the required properties of a NAADP-BP dependent Ca^{2+} release mechanism (*14, 35*), JPT2 binds NAADP with nanomolar affinity (Fig. 5), associates with TPC1 (Fig. 6A) and is required for NAADP-evoked Ca^{2+} signals in U2OS cells (Fig. 6, B and C) and NAADP-dependent trafficking processes (Fig. 7). These data establish JPT2 as an essential component of a NAADP-BP complex that confers endogenous NAADP sensitivity to TPCs.

JPT2 (also known as hematological and neurological expressed 1-like, HN1L) was originally identified in a mouse fertilized egg library (*21*) and is broadly expressed in human primary tissues and cell lines (Fig. 2G, (*11, 19-21, 36*)). The JPT gene family (JPT1 [HN1] and JPT2 [HN1-L]) is also evolutionarily conserved (Fig. 3B, (*21*)) although comparatively little is known about the roles of these family members. JPT2 contains many positively charged residues which may be relevant for NAADP binding, given the presence of negatively charged pyrophosphate,

phosphate and carboxylate group in NAADP at physiological pH. Further work will be needed to define this interaction in detail, and the resemblance of the repeated motifs in JPT2 to canonical NA(A)DP binding sequences (*37*).

Using T cells, Roggenkamp *et al.* also identify HN1L/JPT2 as a photolabeled NAADP-BP (*38*), that is critical for the generation of localized Ca^{2+} microdomains observed in the earliest phases of T cell activation (*39*). These localized Ca^{2+} microdomains appear to be dependent on NAADP-dependent activation of the ryanodine receptor isoform 1 (RyR1) in the ER (*40*). Knockdown of *HN1L/JPT2* in both human Jurkat cells as well as rat primary T cells impaired local, and consequently global Ca^{2+} signals evoked by T cell receptor and CD3 stimulation (*39*). Therefore, studies performed in different cell types both converge to implicate JPT2 as a component of NAADP receptor but diverge in their observations that JPT2 confers NAADP sensitivity to different types of intracellular Ca^{2+} channel: TPCs (this study) or RyRs (*38*). The hypothesis that NAADP-BPs may act to confer NAADP-sensitivity to different families of intracellular Ca^{2+} channel, an attractive idea in this field for over a decade (*14, 35, 41*), receives clear experimental support from this pair of studies.

Considering the shared pedigree between TPCs and other members of the voltage-gated ion channel family (Ca_v, Na_v, K_v, (*42*)), the idea of a multifunctional NAADP-BP accessory subunit is not unreasonable. The function of each major subfamily of voltage-operated channels is modulated by accessory subunits (*14*). Many of these accessory protein subunits are promiscuous with physiological roles dependent on, and independent from, their ion channel

partners. Many ion channel accessory proteins have ligand binding sites, for example IP_3Rs and RyRs (FKBPs, (*43*)), Ca_v ($\alpha_2\delta$ subunits, (*44*)) and K^+ channels (K_{ATP}, nucleotides, (*45*); Kv1.4, sigma receptors (*46*)). One pertinent example is the Na_v channel β subunit, which is both promiscuous and fulfills physiological roles independent from the pore-forming subunit in both excitable and non-excitable cells (*47*). This provides precedent for JPT2 acting independently from TPCs (in organisms such as *Drosophila* lacking TPCs, Fig. 3B) or TPCs functioning without NAADP-activation (acting solely as $PI(3,5)P_2$-gated channels (*10*)). The ability for JPT2 to associate with both TPC1 and RyR1 is also intriguing in the context of close coupling of these ion channels at tightly apposed membrane contact sites between acidic Ca^{2+} stores and the ER that amplify local NAADP-evoked Ca^{2+} signals into global, whole cell Ca^{2+} signals (*48*). The preferential association of JPT2 with TPC1 compared with TPC2 also raises the possibility that multiple NAADP-BPs may exist to confer NAADP sensitivity, and possibly unique functionalities to TPC isoforms. Identification of JPT2 now provides a molecular handle to interrogate these possibilities.

The identification of JPT2 as the photolabeled NAADP-BP also implicates a role of NAADP-evoked Ca^{2+} signaling in processes where a functional requirement for JPT2/HN1L has been already established. JPT2 has been shown to interact with multiple signaling pathways (*49-51*), but one consistent theme is a role in cell growth and tumorigenesis. JPT2 overexpression stimulates cell proliferation, tumor growth and metastasis, whereas JPT2 knockdown suppresses cell growth and migration (*49-51*). JPT2 expression is elevated in cancer tissues compared with matched controls and this upregulation correlates with poorer patient survival

outcomes in several types of cancer (*49-52*), including non-small cell lung cancer (*49*), hepatocellular carcinoma (*50*) and triple negative breast cancer (*51*). These findings are of special interest given an emerging focus on NAADP-evoked Ca^{2+} signaling in cancer cell growth (*8, 53, 54*).

A second area of pathophysiological relevance, underscored by our data (Fig. 6), relates to viral infection. A role for JPT2/HN1L in the inhibition of apoptosis in response to viral infection has previously been demonstrated (*27*). JPT2/HN1L has also been localized to Nipah viral particles (a zoonotic paramyxovirus) within host cells (*55*). Here, we show that JPT2 supports the endolysosomal translocation but not direct entry of a SARS-CoV-2 pseudovirus (Fig. 7B), data which extends our previous discovery of a role of the TPC complex in coronaviral infectivity (*5, 30*). Pharmacological blockade of NAADP-evoked Ca^{2+} release (*5, 32*) or knockdown of JPT2 (Fig. 7B) has now been evidenced to impair the endolysosomal translocation of two, different coronaviral spike proteins (MERS, SARS-CoV-2). Given the endolysosomal processing of SARS-CoV-2 resembles that of MERS-CoV (*31*), this is not unexpected and provided good rationale to identify ligands that block JPT2 function and NAADP action as broader anti-CoV therapeutics (*7*). This additional insight into the role of the JPT2/TPC complex in SARS-CoV-2 translocation holds particular significance given the current COVID-19 pandemic which has infected >35 million people, with more than a million fatalities at the time of writing.

In summary, identification of JPT2 will further our understanding of the mechanism of NAADP action, aiding analysis of how NAADP sensitivity is conferred to TPCs and possibly other

intracellular Ca^{2+} channels (*14, 35*). Resolution of JPT2 as an endogenous mediator of NAADP signaling also opens new opportunity to understand the roles of this understudied gene family in Ca^{2+} signaling processes in both normal physiology and disease states.

Materials and Methods

Synthesis of alkyne-AIOC-NAADP. The bifunctional nicotinic acid derivative **1** was prepared by coupling 3-azido-5-alkynyl-benzoic acid (**2**) (*56, 57*) and 5-(3-aminopropyl)-nicotinic acid ethyl ester (**3**) (*58*) forming ester **4** followed by ester hydrolysis (Scheme 1). Alkyne-AIOC-NAADP was synthesized from **1** and NADP using the pyridine base exchange reaction catalyzed by mutant *Aplysia californica* ADP-ribosyl cyclase [E98G], under previously described conditions (*19*). Samples were purified using methods reported previously (*19*).

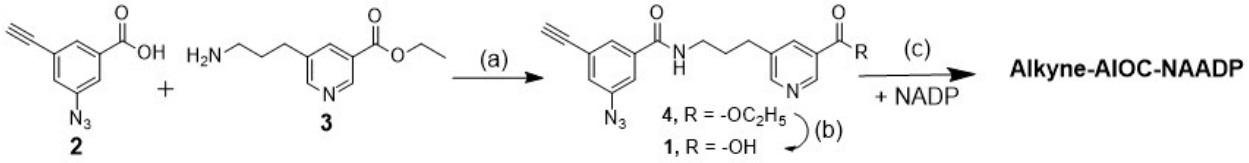

Scheme 1. Synthesis of Alkyne-AIOC-NAADP. Reagents and conditions: (a) PyBOP, DIPEA, DCM, 1 h 81.4%; (b) (1) CH_3OH/tetrahydrofuran 1:1 and KOH (2) 1M HCl; (c) E98G ADP-ribosyl cyclase, pH 7.5, 37°C.

Alkyne-AIOC-NAADP. Compound **4** (75.5 mg, 0.2 mmol) dissolved in 50% CH_3OH-tetrahydrofuran (5 mL) was treated with 1M KOH (4 mL) and stirred until **4** was consumed (TLC on silica gel; 70% Ethyl acetate in hexane) in approximately 3 hours. The pH was adjusted to 7 using 1M HCl (4mL), the mixture concentrated *in vacuo*, re-dissolved in water (5 mL) and the pH of the mixture adjusted to 7.5. NADP (15 mg, 0.02 mmol) was added and the pH was adjusted to 7.5 again. E98G *A. californica* ADP-ribosyl cyclase (0.08 mg, 400 µl) was added, and the resulting mixture was stirred at 37°C. The consumption of NADP was monitored by analytical anion-exchange HPLC. After NAADP was consumed product was isolated by preparative anion-

exchange chromatography using a linear gradient formed between water (solvent A) and 100 mM TFA (solvent B) over 15 minutes to 40% B, followed by a linear gradient starting from 40% B and ending with 85% B over 55 minutes. Under these conditions alkyne-AIOC-NAADP eluted between 37-48 min into 51%-60% B. For spectroscopic characterization the product was collected, frozen at -80 ℃ and lyophilized. Water (3 mL) was added and the solution applied to a DEAE-cellulose column for a second purification developed using a linear gradient formed between water and 800 mM NH_4HCO_3 solution. A single UV (280 nm) absorbing peak was observed, and fractions combined, frozen and lyophilized to give the target compound as white powder (4.51 mg, 23.2%). ^{1}H NMR (600 MHz, D_2O) δ 9.05 (s, 1H), 8.93 (s, 1H), 8.72 (s, 1H), 8.39 (s, 1H), 8.17 (s, 1H), 7.38 (s, 1H), 7.23 (s, 1H), 7.20 (s, 1H), 6.09 (d, J= 5.4 Hz, 1H), 6.03 (d, J= 5.4 Hz, 1H), 3.59(s, 1H), 3.43 (q, J= 7.0 Hz, 2H), 2.99 (t, J= 7.5 Hz, 2H), 2.05 (m, J= 7.2 Hz, 2H), 1.25 (d, J= 14.4 Hz, 1H). ESI-TOF MS calcd for $C_{33}H_{38}N_{10}O_{19}P_3^+$: 971.1528 (M+), 993.1339 (M - H + Na), 1015.1150 (M - 2H + 2Na), 1037.0961 (M - 3H + 3Na). Found m/z :971.1528 (M+), 993.1274 (M - H + Na), 1015.1089 (M - 2H + 2Na), 1037.0906 (M - 3H + 3Na). High specific activity ^{32}P-alkyne-AIOC-NAADP was synthesized in a similar fashion as unlabeled alkyne-AIOC-NAADP by substituting high specific activity ^{32}P-NADP for unlabeled NADP in the base exchange reaction. Details of the synthesis of ^{32}P-NADP and purification have been previously described (*19*).

Synthesis of ethyl 5-(3-(3-azido-5-ethynylbenzamido)propyl)nicotinate (4). 3-Azido-5-ethynylbenzoic acid[1,2] (**2**) (173.2 mg, 0.93 mmol) was dissolved in dichloromethane (8 mL). Ethyl 5-(3-aminopropyl)nicotinate (**3**) (488.65 mg, 1.12 mmol), PyBOP (484 mg, 0.93 mmol; Sigma-

Aldrich Chemicals #377848) and diisopropylethylamine (1 mL; Acros Chemicals #367841000) was added. The resulting mixture was stirred at room temperature until the starting material was consumed (TLC, silica gel; 70% ethyl acetate in hexane). The reaction mixture was concentrated and purified by column chromatography (silica gel; 40 to 70% ethyl acetate to give white solid **4** (284.1 mg, 81.4% yield); TLC R_f 0.36 in 70 % Ethyl acetate in hexanes; mp 109-112 °C; ^{1}H NMR (600 MHz, $CDCl_3$) δ 9.04 (s, 1H), 8.60 (d, J = 2.4 Hz, 1H), 8.12 (d, J= 1.8 Hz, 1H), 7.56 (t, J= 1.5 Hz, 1H), 7.43 (t, J= 1.5 Hz, 1H), 7.20 (t, J= 0.9 Hz, 1H), 6.88 (s, 1H), 4.40 (q, J= 7.2 Hz, 2H), 3.51 (q, J= 6.8 Hz, 2H), 3.16 (s, 1H), 2.76(t, J= 7.8 Hz, 2H), 1.98 (t, J= 7.8 Hz, 2H), 1.40 (t, J= 7.2 Hz, 3H); ^{13}C-NMR (600 MHz, $CDCl_3$) δ 165.98, 165.37, 153.32, 148.66, 141.07, 136.66, 136.59, 136.51, 126.57, 126.13, 124.89, 124.09, 118.45, 81.67, 79.26, 61.52, 39.74, 30.79, 30.20, 14.28; ESI-TOF HRMS calcd for $C_{20}H_{19}N_5O_3$: 378.1566 (M + H), 400.1371 (M + Na). Found m/z: 378.1584 (M + H), 400.1517 (M + Na). Anal. Calcd for $C_{20}H_{19}O_3N_5$ • 0.2 ethyl acetate: C, 63.24; H, 5.26; N,17.73. Found: C, 63.19; H, 5.28; N, 17.87.

Sample preparation. Human erythrocytes were collected from outdated blood bags supplied by the University of Minnesota Blood Bank Laboratory. Erythrocytes were washed 3 times in 0.9% saline solution. Packed erythrocytes were then lysed in 3 volumes of hypotonic solution of 10mM Tris-HCl, pH 8.5, supplemented with cOmplete EDTA-free protease inhibitor cocktail (Roche). Erythrocyte lysate was centrifuged at 20,000xRCF for 30 minutes, supernatant (S20) was reserved for further processing. Protein concentration was determined by Bradford assay (Thermo Scientific). Jurkat, U2OS, and HEK293 lysates were prepared as previously described (*16, 18, 20*). Briefly, cells were washed with PBS and collected by centrifugation and scraping.

Cell pellets were suspended in 20mM HEPES, pH 7.4 supplemented with protease inhibitors. Cell suspensions were sonicated to produce whole cell lysates, and subsequently centrifuged at 200,000xRCF. Supernatant (S200) fractions were collected for analysis.

Photoaffinity labeling of NAADP-BPs. When determining a scheme for chromatographic enrichment of NAADP binding proteins, 5µg of fractionated protein was incubated with ^{32}P-alkyne-AIOC-NAADP at a final concentration of 1-7nM, reactions were incubated on ice for 1 hour prior to 2 minutes of ultraviolet irradiation. When photolabeling protein prior to click chemistry-based purification, fractionated protein was separately incubated with either alkyne-AIOC-NAADP at a final concentration of 1µM or incubated with ^{32}P-alkyne-AIOC-NAADP at a final concentration of 5nM. All reactions were incubated on ice for 1 hour prior to 2 minutes of ultraviolet irradiation. Reactions with then mixed prior to click chemistry experiments. Photolabeled protein was then incubated (<15min) with SDS sample buffer supplemented with 2-mercaptoethanol (10%). Samples were then separated by SDS-PAGE on 12% TGX gels (BioRad). Gels were silver stained using ProteoSilver (Sigma Aldrich) and air-dried. The photolabeling was analyzed by exposing the dried gels to MP storage phosphor screens (Packard Instruments). The screens were developed using a Typhoon storage phosphor system. Densitometric analysis was accomplished using Image J software.

Chromatographic enrichment of NAADP-BPs. Human erythrocyte S20 supernatant was fractionated over various resins as follows: For anion exchange chromatography, a column of Q Sepharose Fast Flow (GE Healthcare) resin was equilibrated with 10mM HEPES, pH 8.5. Protein

samples were pumped onto the column, approximately 50mg of protein/ml resin. Retained protein was washed with 3 column volumes of 10mM HEPES + 50mM NaCl, pH 8.5. Protein was eluted with 10mM HEPES + 150mM NaCl, pH 8.5. For cation exchange chromatography, a column of SP Sepharose Fast Flow (GE Healthcare) resin was equilibrated with 10mM HEPES, pH 7.0. Protein samples were adjusted to pH 7.0 and pumped onto the column, approximately 50mg/ml resin. Retained protein was washed with 3 column volumes of 10mM HEPES + 30mM NaCl, pH 7.0. Protein was eluted with 10mM HEPES + 100mM NaCl, pH 7.0. For hydrophobic interaction chromatography (HIC), Phenyl-Sepharose CL-4B (GE Healthcare) resin was equilibrated with 1.5M $(NH_4)_2SO_4$, pH 7.0. Protein samples were supplemented with 1.5M $(NH_4)_2SO_4$ and pumped onto column. Retained protein was washed with 3 column volumes of 1.5M $(NH_4)_2SO_4$, pH 7.0, protein was eluted in 600mM $(NH_4)_2SO_4$, pH 7.0. For Fe^{3+}-NTA fractionation, Ni^{2+}-NTA resin (Qiagen) was stripped according to vendor protocols and re-charged with 0.2M $FeSO_4$. Fe^{3+}-NTA resin was equilibrated with 300mM NaCl + 5mM imidazole, 50mM HEPES, pH 8.0. Protein samples were diluted 1:10 in equilibration buffer and pumped onto column. Column was washed with 5 volumes of equilibration buffer, flowthrough was collected. For “serial” chromatography, approximately 8g of RBC S20 was sequentially fractionated over Q, SP, Phenyl, and NTA resins, in this order. Samples were desalted and concentrated using Amicon Ultra 3kDa MWCO spin filters between each step. Phosphoprotein Enrichment Kit (Pierce) was used for the final stage of enrichment, following vendor protocol. Protein was incubated with phosphoprotein enrichment resin, flowthrough and eluates were collected. Samples were desalted and concentrated prior to photoaffinity labeling as described

above. Photolabeled protein samples were then incubated with fresh phosphoprotein enrichment resin for a second time, collecting subsequent flowthrough and eluate fractions.

Click chemistry and capture of NAADP-BPs. After sequential chromatographic fractionation and enrichment, protein samples with probe-bound NAADP-binding proteins were biotinylated using click chemistry. Approximately 250µg of protein was diluted into 20mM HEPES, pH 7.4, and supplemented with either 10 µM Dde-biotin-picolyl-azide, 10µM biotin-azide-Plus or DMSO. A 40x stock of 60mM BTTAA and 12mM Cu_2SO_4 was prepared in a separate tube. Click reactions were then sequentially supplemented with 5mM aminoguanidine, 1.5mM BTTAA/300µM $CuSO_4$, and 5mM ascorbic acid, with brief vortexing after each addition. Reactions were incubated for 2 hours at room temperature in an end-over-end mixer. Click reagents were removed by buffer exchange, using 3kDa MWCO ultrafiltration spin columns. Biotinylated protein was captured using 100µl of Neutravidin agarose beads (Thermo Scientific) at 4˚C overnight in an end-over-end mixer. Beads were washed twice with RIPA buffer (50mM Tris base, pH 8.0, 150mM NaCl, 0.1% SDS, 1% triton-X-100, 0.5% deoxycholate), twice with PBS + 1% triton-X-100, once with 1M KCl, twice with 100mM $NaCO_3$ pH 11.5 (excluded with Dde-biotin-picolyl azide samples and corresponding controls), twice with 2M urea, once with RIPA, and three times with PBS. Proteins from CuAAC reactions using Dde-biotin-picolyl-azide and corresponding controls were eluted by suspending samples in 3% hydrazine + 0.05% SDS and incubating for 30min at room temperature in an end-over-end mixer. Proteins from CuAAC reactions using biotin-azide-Plus and corresponding controls were eluted by suspending samples in 10mM D(+)-biotin + 10mM EDTA and incubated in a water bath at 90˚C for 10min.

Supernatants from both sets of reactions were collected, and elution was repeated two more times. Eluates were concentrated and buffer exchanged to 20mM HEPES, pH 7.4 using 3kDa MWCO spin columns. Eluates were then separated by SDS-PAGE using a 12% Critereon TGX gel and silver stained. The gels were dried overnight and mounted on a phosphorscreen for detection of radiolabeled NAADP binding proteins. Silver-stained bands that aligned with ^{32}P signals were excised and analyzed by mass spectrometry, along with corresponding bands from non-biotinylated click control samples and input samples.

Mass spectrometry. Proteomic analysis of gel bands was conducted by MS BioWorks (Ann Arbor, Michigan). In-gel digestion was performed using a ProGest robot (DigiLab) with the following protocol: samples were washed with 25mM NH_4HCO_3 followed by acetonitrile, reduced with 10mM dithiothreitol at 60°C, alkylated with 50mM iodoacetamide at room temperature. Samples were digested with trypsin (Promega) at 37°C for 4 hours. Digestions were quenched with formic acid and supernatants collected for analysis. Half of each digested sample was analyzed by nano LC-MS/MS with a Waters M-Class HPLC system interfaced to a ThermoFisher Fusion Lumos mass spectrometer. Peptides were loaded on a trapping column and eluted over a 75µm analytical column at 350nL/min; both columns were packed with Luna C18 resin (Phenomenex). The mass spectrometer was operated in data-dependent mode, with the Orbitrap operating at 60,000 FWHM and 15,000 FWHM for MS and MS/MS respectively. The instrument was run with a 3s cycle for MS and MS/MS. Data were searched using a local copy of Mascot (Matrix Science) with the following parameters: Enzyme - Trypsin/P, Databases - SwissProt Human (concatenated forward and reverse plus common contaminants), Fixed

modifications - Carbamidomethyl (C), Variable modifications - Acetyl (N-term), Deamidation (N,Q), Oxidation (M), Pyro-Glu (N-term Q), Mass values – Monoisotopic, Peptide Mass Tolerance - 10 ppm, Fragment Mass Tolerance - 0.02 Da, Max Missed Cleavages – 2. Mascot DAT files were parsed into Scaffold (Proteome Software) for validation, filtering and to create a non-redundant list per sample. Data were filtered using at 1% protein and peptide FDR and requiring at least two unique peptides per protein. Relative protein abundance was assessed by calculating normalized spectral abundance factor (NSAF) values (*59*).

$$(\mathrm{NSAF})_k = \frac{\left(\frac{\mathrm{SpC}}{\mathrm{Mw}}\right)_k}{\sum_{i=1}^{n}\left(\frac{\mathrm{SpC}}{\mathrm{Mw}}\right)}$$

Briefly, total spectral counts (SpC) for an identified protein (k) were normalized to protein size by dividing spectral counts by the predicted mass of the intact protein (M_W), yielding a spectral abundance factor (SAF). Next, SAF values for individual identified proteins were divided by the sum of all SAF values for each identified protein in a given biological sample (n).

Cell culture and transfection. Jurkat cells were maintained in RPMI medium, U2OS and HEK293 cells were maintained in DMEM. Cell culture medium was supplemented with 10% fetal bovine serum, 100 units/ml penicillin and streptomycin, and 292 µg/ml L-glutamine, and cells were cultured at 5% CO_2 and 37°C. For plasmid transfection, $3.5x10^5$ U2OS or HEK293 cells were seeded in a 35mm well in the absence of antibiotics. The following day, cells were transfected with siRNA (1-20nM) using RNAiMax (Thermo) according to the vendor's protocol. Media was

changed 24 hours post transfection and cells were harvested by scraping 48 hours post transfection.

Calcium imaging. U2OS Cells were incubated with fura-2 AM (5 µM, Invitrogen) in Hanks' balanced salt solution (HBSS, room temperature, 45 min in the dark), washed, and incubated for another 45 min to allow for de-esterification. Coverslips were mounted in a custom-designed bath on the stage of an inverted microscope (Nikon Eclipse TE 2000-U, 40× NA 1.3 oil immersion objective). Cells were superfused (flow rate, ~0.5 ml/min) with HBSS and fluorescence emission (510nm) captured with a charge-coupled device camera (Roper Scientific) after alternate excitation at 340 and 380 nm. Captured images were analyzed using MetaFluor software. Single cell microinjections were performed as previously described (*11*) using Femtotips II, an InjectMan NI 2 and a Femtojet systems (Eppendorf). Pipettes were back filled with an intracellular solution composed of 110mM KCl, 10mM NaCl and 20 mM Hepes, pH 7.2, and supplemented with NAADP (10µM). siRNA transfected cells were selected by identifying cells displaying similar intensities of GFP fluorescence.

Immunoblotting and immunoprecipitation. For immunoprecipitation of photolabeled NAADP-BPs, erythrocyte S20 and U2OS S200 lysates were incubated with either 2µg/ml rabbit IgG isotype control antibody (Thermo Scientific), 0.5µg/ml anti-HN1L antibody produced in rabbit (Sigma Aldrich, HPA041908, 'anti-JPT2 #1'), or 2µg/ml anti-HN1L antibody produced in rabbit (Thermo Scientific, PA5-59774, 'anti-JPT2 #2') at 4°C for 1 hour before an overnight incubation with protein-G agarose beads (Roche). For co-immunoprecipitation experiments, HEK293 cells

overexpressing TPC1-GFP or TPC2-GFP were solubilized in buffer composed of 110mM KCl, 10µM $CaCl_2$, 1% Triton X-100, 20mM HEPES, pH7.4 supplemented with Halt phosphatase inhibitor (Pierce) and cOmplete EDTA-free protease inhibitor cocktail (Roche). Lysates were centrifuged at 16,000xRCF for 10min/4°C, and supernatant was collected. 1mg of solubilized lysate was incubated with 2µg/ml of either rabbit IgG isotype control antibody, anti-GFP antibody produced in rabbit (Thermo Scientific, G10362), or anti-HN1L antibody produced in rabbit (Sigma Aldrich, HPA041908 at 4˚C for 1 hour before an overnight incubation with protein-G agarose beads (Roche). Beads were collected after brief centrifugation and were washed three times with PBS + 1% Triton X-100. For photolabeling experiments, immunoprecipitated protein was eluted by rinsing beads three times with 0.2M glycine pH 2.6 for 1min, rinses were immediately neutralized with 2M Tris base followed by concentration and desalting. For Co-IP experiments, immunoprecipitated complexes were eluted by incubating beads with 2x Laemmli sample buffer at 95°C for 10min. For immunodetection of proteins, 20µg of HEK293 or U2OS whole-cell lysate was separated by SDS-PAGE and transferred to nitrocellulose membranes using standard methods. Nitrocellulose membranes were blocked in 5% milk in tris buffered saline supplemented with 0.1% tween-20 for 1 hour at room temperature. Membranes were then incubated with primary antibodies at a concentration of 0.05µg/ml (anti-HN1L, Sigma Aldrich, HPA041908 and anti-GAPDH, Santa Cruz Biotechnology, sc-47724) overnight at 4˚C. The following day membranes were incubated with IRDye secondary antibodies (1:5000 dilution, LI-COR) for 1 hour at room temperature. Signals were detected using a LI-COR Odyssey Imaging system.

Production of recombinant JPT2. cDNA encoding JPT2 (Uniprot ID# Q9H910-3) fused with an N-terminal 6xHis-GST-TEV protease cleavage site was subcloned into pGS-21a bacterial expression vector and transformed into BL21 Star (DE3) *E. coli* cells. A single colony was inoculated into TB medium and cultured at 37°C. When the OD_{600} reached 1.2, the culture was induced with IPTG at 15°C/16h. Cells were harvested by centrifugation and cell pellets were resuspended with lysis buffer followed by sonication. Protein was loaded onto a Ni-NTA column and 6xHis-GST-TEV-JPT2 was eluted with 400mM imidazole. Protein was treated with TEV protease to remove N-terminal tags, and untagged JPT2 was collected by loading onto a Ni-NTA column and eluting with 10mM imidazole, samples were concentrated, and buffer exchanged using 20mM HEPES pH 7.4 and 3kDa MWCO ultrafiltration spin columns.

^{32}P-NAADP binding assays. Recombinant JPT2 (20µg) was incubated with [^{32}P]-NAADP (~0.33nM) in the presence of increasing concentrations of cold NAADP or NADP for 1 hour on ice. During the incubation, multiScreen-IP 96-well PVDF plates (Millipore) were mounted on a vacuum manifold. PVDF membranes were wetted with ethanol, followed by two washes with 20mM HEPES, pH 7.4. Binding reactions were transferred to 96-well PVDF plates and filtered through PVDF membranes. Membranes were washed 3 times with ice-cold 20mM HEPES, pH 7.4. Rubber gaskets were removed from the underside of 96-well PVDF plates, and PVDF wells were dried with paper towels. PVDF plates were then placed on phosphor screens, subsequently processed using a Typhoon phosphor storage system. Bound [^{32}P]-NAADP was quantified by densitometry using ImageJ.

SARS-Cov-2 pseudovirus translocation assays. Cell infection assays were carried out as described previously for MERS-CoV (*5, 60*). Spike-pseudotyped retroviruses expressing a luciferase reporter gene were prepared by co-transfecting HEK293T cells with a plasmid carrying Env-defective, luciferase-expressing HIV-1 genome (pNL4-3.luc.RE) and a plasmid encoding SARS-CoV-2 spike (S) protein, which is necessary and sufficient to facilitate cell entry. SARS-CoV-2 pseudovirus particles were harvested from supernatant 72hrs after transfection. HEK-293 cells (overexpressing ACE2) were used to monitor SARS-CoV-2 pseudovirus translocation. Cells were seeded into 96-well plates (Midwest Scientific) at a concentration of $1x10^4$ cells/well. The following day, cells were pre-incubated with individual drugs (10µM, final concentration) for 1 hour prior to pseudovirus addition. Cells were incubated (5% CO_2/37°C) for an additional 5 hours in the presence of drug and pseudovirus. After 6hrs, the culture media was replaced with complete DMEM and cells were incubated for a further 60hrs. Cells were then washed 3 times with DPBS (Invitrogen) and assayed for luciferase activity. Cells were lysed in 80µl lysis buffer (Promega) per well, and 40µl of lysate was transferred to solid-white 96-well plates (Corning) and mixed with 40µl of luciferase substrate (Promega). Luminescence (relative luminescence units, RLUs) were measured using a Tecan Infinite M100 microplate reader. Luminescence values are reported relative to values measured in cells treated with virus alone, background corrected by luminescence values in cells unexposed to virus, except where indicated.

Statistical analysis. A univariate regression model with type as a categorical covariate was used to evaluate differences in intensity between type of samples. Type was coded as a categorical

variable with the reference category being the control state or appropriate group against which others were being compared. The coefficients calculated from this regression model were used to calculate the *P* statistic (* $P<0.05$, ** $P<0.01$, *** $P<0.005$).

Chemicals and molecular reagents. NAADP was synthesized by incubating nicotinamide adenine dinucleotide phosphate (NADP, Sigma-Aldrich) with nicotinic acid in the presence of recombinant *Aplysia* ADP-ribosyl cyclase (*61*) followed by high-performance liquid chromatography (HPLC) purification. NADP was freshly purified by HPLC prior to experimentation to remove contaminating NAADP (*17*). Nicotinic acid, nicotinamide, nicotinamide adenine dinucleotide (NAD), nicotinic acid adenine dinucleotide sodium salt (NAAD), adenosine 5'-triphosphate disodium salt hydrate (ATP), β-nicotinamide ribose monophosphate (β-NMN) and D(+)-biotin were purchased from Sigma Aldrich. 2-[4-((bis[(1-tert-butyl-1H-1,2,3-triazol-4-yl)methyl]amino)methyl)-1H-1,2,3-triazol-1-yl]acetic acid (BTTAA), Dde-biotin-picolyl-azide and biotin-azide-Plus were purchased from Click Chemistry Tools (Scottsdale, AZ). Silencer Select siRNAs targeted against JPT2 and non-targeting negative control siRNAs were purchased from Thermo Scientific. siRNA sequences were: JPT2 siRNA #1 – GAACCAAAAUCGGAUCUUAtt, JPT2 siRNA #2 – CCAAGGAUCAUGUUUUCUUtt.

Supplementary Materials

Fig. S1. Chromatographic enrichment of NAADP-BP.

Fig. S2. Validation of knockdown methods.

References and Notes

1. S. Patel, L. Ramakrishnan, T. Rahman, A. Hamdoun, J. S. Marchant, C. W. Taylor, E. Brailoiu, The endo-lysosomal system as an NAADP-sensitive acidic Ca^{2+} store: Role for the two-pore channels. *Cell Calcium* **50**, 157-167 (2011).
2. H. C. Lee, Cyclic ADP-ribose and nicotinic acid adenine dinucleotide phosphate (NAADP) as messengers for calcium mobilization. *J. Biol. Chem.* **287**, 31633-31640 (2012).
3. A. Galione, A primer of NAADP-mediated Ca^{2+} signalling: from sea urchin eggs to mammalian cells. *Cell Calcium* **58**, 27-47 (2015).
4. Y. Sakurai, A. A. Kolokoltsov, C. C. Chen, M. W. Tidwell, W. E. Bauta, N. Klugbauer, C. Grimm, C. Wahl-Schott, M. Biel, R. A. Davey, Ebola virus. Two-pore channels control Ebola virus host cell entry and are drug targets for disease treatment. *Science* **347**, 995-998 (2015).
5. G. S. Gunaratne, Y. Yang, F. Li, T. F. Walseth, J. S. Marchant, NAADP-dependent Ca(2+) signaling regulates Middle East respiratory syndrome-coronavirus pseudovirus translocation through the endolysosomal system. *Cell Calcium* **75**, 30-41 (2018).
6. N. Khan, P. W. Halcrow, K. L. Lakpa, Z. Afghah, N. M. Miller, S. F. Dowdy, J. D. Geiger, X. Chen, Two-pore channels regulate Tat endolysosome escape and Tat-mediated HIV-1 LTR transactivation. *FASEB J.* **34**, 4147-4162 (2020).
7. C. Grimm, R. Tang, Could an endo-lysosomal ion channel be the Achilles heel of SARS-CoV2? *Cell Calcium* **88**, 102212 (2020).
8. S. Patel, B. S. Kilpatrick, Two-pore channels and disease. *Biochim Biophys Acta Mol Cell Res* **1865**, 1678-1686 (2018).
9. M. Ruas, L. C. Davis, C. C. Chen, A. J. Morgan, K. T. Chuang, T. F. Walseth, C. Grimm, C. Garnham, T. Powell, N. Platt, F. M. Platt, M. Biel, C. Wahl-Schott, J. Parrington, A. Galione, Expression of Ca(2)(+)-permeable two-pore channels rescues NAADP signalling in TPC-deficient cells. *EMBO J.* **34**, 1743-1758 (2015).
10. S. Gerndt, C. C. Chen, Y. K. Chao, Y. Yuan, S. Burgstaller, A. Scotto Rosato, E. Krogsaeter, N. Urban, K. Jacob, O. N. P. Nguyen, M. T. Miller, M. Keller, A. M. Vollmar, T. Gudermann, S. Zierler, J. Schredelseker, M. Schaefer, M. Biel, R. Malli, C. Wahl-Schott, F. Bracher, S. Patel, C. Grimm, Agonist-mediated switching of ion selectivity in TPC2 differentially promotes lysosomal function. *eLife* **9**, 10.7554/eLife.54712 (2020).
11. E. Brailoiu, D. Churamani, X. Cai, M. G. Schrlau, G. C. Brailoiu, X. Gao, R. Hooper, M. J. Boulware, N. J. Dun, J. S. Marchant, S. Patel, Essential requirement for two-pore channel 1 in NAADP-mediated calcium signaling. *J. Cell Biol.* **186**, 201-209 (2009).
12. P. J. Calcraft, M. Ruas, Z. Pan, X. Cheng, A. Arredouani, X. Hao, J. Tang, K. Rietdorf, L. Teboul, K. T. Chuang, P. Lin, R. Xiao, C. Wang, Y. Zhu, Y. Lin, C. N. Wyatt, J. Parrington, J. Ma, A. M. Evans, A. Galione, M. X. Zhu, NAADP mobilizes calcium from acidic organelles through two-pore channels. *Nature* **459**, 596-600 (2009).
13. X. Zong, M. Schieder, H. Cuny, S. Fenske, C. Gruner, K. Rotzer, O. Griesbeck, H. Harz, M. Biel, C. Wahl-Schott, The two-pore channel TPCN2 mediates NAADP-dependent Ca(2+)-release from lysosomal stores. *Pflugers Arch.* **458**, 891-899 (2009).

14. J. S. Marchant, Y. Lin-Moshier, T. F. Walseth, S. Patel, The Molecular Basis for Ca(2+) Signalling by NAADP: Two-Pore Channels in a Complex? *Messenger (Los Angel)* **1**, 63-76 (2012).
15. I. M. Wolf, B. P. Diercks, E. Gattkowski, F. Czarniak, J. Kempski, R. Werner, D. Schetelig, H. W. Mittrucker, V. Schumacher, M. von Osten, D. Lodygin, A. Flugel, R. Fliegert, A. H. Guse, Frontrunners of T cell activation: Initial, localized Ca2+ signals mediated by NAADP and the type 1 ryanodine receptor. *Sci Signal* **8**, ra102 (2015).
16. Y. Lin-Moshier, T. F. Walseth, D. Churamani, S. M. Davidson, J. T. Slama, R. Hooper, E. Brailoiu, S. Patel, J. S. Marchant, Photoaffinity labeling of nicotinic acid adenine dinucleotide phosphate (NAADP) targets in mammalian cells. *J. Biol. Chem.* **287**, 2296-2307 (2012).
17. T. F. Walseth, Y. Lin-Moshier, P. Jain, M. Ruas, J. Parrington, A. Galione, J. S. Marchant, J. T. Slama, Photoaffinity labeling of high affinity nicotinic acid adenine dinucleotide phosphate (NAADP)-binding proteins in sea urchin egg. *J. Biol. Chem.* **287**, 2308-2315 (2012).
18. T. F. Walseth, Y. Lin-Moshier, K. Weber, J. S. Marchant, J. T. Slama, A. H. Guse, Nicotinic Acid Adenine Dinucleotide 2'-Phosphate (NAADP) Binding Proteins in T-Lymphocytes. *Messenger (Los Angel)* **1**, 86-94 (2012).
19. T. Y. Asfaha, G. S. Gunaratne, M. E. Johns, J. S. Marchant, T. F. Walseth, J. T. Slama, The synthesis and characterization of a clickable-photoactive NAADP analog active in human cells. *Cell Calcium* **83**, 102060 (2019).
20. G. S. Gunaratne, P. Su, J. S. Marchant, J. T. Slama, T. F. Walseth, 5-Azido-8-ethynyl-NAADP: A bifunctional, clickable photoaffinity probe for the identification of NAADP receptors. *Biochim Biophys Acta Mol Cell Res* **1866**, 1180-1188 (2019).
21. G. Zhou, J. Wang, Y. Zhang, C. Zhong, J. Ni, L. Wang, J. Guo, K. Zhang, L. Yu, S. Zhao, Cloning, expression and subcellular localization of HN1 and HN1L genes, as well as characterization of their orthologs, defining an evolutionarily conserved gene family. *Gene* **331**, 115-123 (2004).
22. H. C. Lee, R. Aarhus, A derivative of NADP mobilizes calcium stores insensitive to inositol trisphosphate and cyclic ADP-ribose. *J. Biol. Chem.* **270**, 2152-2157 (1995).
23. M. Albrieux, H. C. Lee, M. Villaz, Calcium signaling by cyclic ADP-ribose, NAADP, and inositol trisphosphate are involved in distinct functions in ascidian oocytes. *J. Biol. Chem.* **273**, 14566-14574 (1998).
24. L. Santella, K. Kyozuka, A. A. Genazzani, L. De Riso, E. Carafoli, Nicotinic acid adenine dinucleotide phosphate-induced Ca(2+) release. Interactions among distinct Ca(2+) mobilizing mechanisms in starfish oocytes. *J. Biol. Chem.* **275**, 8301-8306 (2000).
25. S. Bezin, G. Charpentier, H. C. Lee, G. Baux, P. Fossier, J. M. Cancela, Regulation of nuclear Ca2+ signaling by translocation of the Ca2+ messenger synthesizing enzyme ADP-ribosyl cyclase during neuronal depolarization. *J. Biol. Chem.* **283**, 27859-27870 (2008).
26. N. Karpova, Y. Bobinnec, S. Fouix, P. Huitorel, A. Debec, Jupiter, a new Drosophila protein associated with microtubules. *Cell Motil. Cytoskeleton* **63**, 301-312 (2006).
27. J. Lei, D. Hu, S. Xue, F. Mao, E. Obeng, Y. Quan, W. Yu, HN1L is essential for cell growth and survival during nucleopolyhedrovirus infection in silkworm, Bombyx mori. *PLoS One* **14**, e0216719 (2019).

28. Z. B. Liu, N. E. Ezzedine, A. K. Eterovic, J. E. Ensor, H. J. Huang, J. Albanell, D. S. Choi, A. Lluch, Y. Liu, F. Rojo, H. Wong, E. Martinez-Duenas, A. Guerrero-Zotano, Z. M. Shao, J. G. Darcourt, G. B. Mills, B. Dave, J. C. Chang, Detection of breast cancer stem cell gene mutations in circulating free DNA during the evolution of metastases. *Breast Cancer Res. Treat.* **178**, 251-261 (2019).
29. C. J. Penny, K. Vassileva, A. Jha, Y. Yuan, X. Chee, E. Yates, M. Mazzon, B. S. Kilpatrick, S. Muallem, M. Marsh, T. Rahman, S. Patel, Mining of Ebola virus entry inhibitors identifies approved drugs as two-pore channel pore blockers. *Biochim Biophys Acta Mol Cell Res* **1866**, 1151-1161 (2019).
30. G. S. Gunaratne, M. E. Johns, H. M. Hintz, T. F. Walseth, J. S. Marchant, A screening campaign in sea urchin egg homogenate as a platform for discovering modulators of NAADP-dependent Ca(2+) signaling in human cells. *Cell Calcium* **75**, 42-52 (2018).
31. J. Shang, Y. Wan, C. Luo, G. Ye, Q. Geng, A. Auerbach, F. Li, Cell entry mechanisms of SARS-CoV-2. *Proc. Natl. Acad. Sci. U. S. A.* **117**, 11727-11734 (2020).
32. X. Ou, Y. Liu, X. Lei, P. Li, D. Mi, L. Ren, L. Guo, R. Guo, T. Chen, J. Hu, Z. Xiang, Z. Mu, X. Chen, J. Chen, K. Hu, Q. Jin, J. Wang, Z. Qian, Characterization of spike glycoprotein of SARS-CoV-2 on virus entry and its immune cross-reactivity with SARS-CoV. *Nature communications* **11**, 1620 (2020).
33. M. Moras, S. D. Lefevre, M. A. Ostuni, From Erythroblasts to Mature Red Blood Cells: Organelle Clearance in Mammals. *Front Physiol* **8**, 1076 (2017).
34. D. Churamani, E. A. Carrey, G. D. Dickinson, S. Patel, Determination of cellular nicotinic acid-adenine dinucleotide phosphate (NAADP) levels. *Biochem. J.* **380**, 449-454 (2004).
35. A. H. Guse, Linking NAADP to ion channel activity: a unifying hypothesis. *Sci Signal* **5**, pe18 (2012).
36. M. Uhlen, C. Zhang, S. Lee, E. Sjostedt, L. Fagerberg, G. Bidkhori, R. Benfeitas, M. Arif, Z. Liu, F. Edfors, K. Sanli, K. von Feilitzen, P. Oksvold, E. Lundberg, S. Hober, P. Nilsson, J. Mattsson, J. M. Schwenk, H. Brunnstrom, B. Glimelius, T. Sjoblom, P. H. Edqvist, D. Djureinovic, P. Micke, C. Lindskog, A. Mardinoglu, F. Ponten, A pathology atlas of the human cancer transcriptome. *Science* **357**, (2017).
37. Y. H. Hua, C. Y. Wu, K. Sargsyan, C. Lim, Sequence-motif detection of NAD(P)-binding proteins: discovery of a unique antibacterial drug target. *Scientific Reports* **4**, 6471 (2014).
38. H. G. Roggenkamp, I. Khansahib, L. C. Herdnandez, Y. Zhang, D. Lodygin, A. Kruger, F. Gu, F. Mockl, A. Lohndorf, V. Wolters, D. Woike, A. Rosche, A. Bauche, D. Schetelig, R. Werner, H. Schluter, A. V. Failla, R. Fliegert, C. Meier, T. F. Walseth, A. Flugel, B.-P. Diercks, A. H. Guse, HN1L/JPT2: a signaling protein connecting NAADP to Ca^{2+} microdomains. *Science Signaling (under review)*, (2020).
39. B. P. Diercks, R. Werner, P. Weidemuller, F. Czarniak, L. Hernandez, C. Lehmann, A. Rosche, A. Kruger, U. Kaufmann, M. Vaeth, A. V. Failla, B. Zobiak, F. I. Kandil, D. Schetelig, A. Ruthenbeck, C. Meier, D. Lodygin, A. Flugel, D. Ren, I. M. A. Wolf, S. Feske, A. H. Guse, ORAI1, STIM1/2, and RYR1 shape subsecond Ca(2+) microdomains upon T cell activation. *Sci Signal* **11**, (2018).
40. W. Dammermann, B. Zhang, M. Nebel, C. Cordiglieri, F. Odoardi, T. Kirchberger, N. Kawakami, J. Dowden, F. Schmid, K. Dornmair, M. Hohenegger, A. Flugel, A. H. Guse, B. V.

Potter, NAADP-mediated Ca2+ signaling via type 1 ryanodine receptor in T cells revealed by a synthetic NAADP antagonist. *Proc. Natl. Acad. Sci. U. S. A.* **106**, 10678-10683 (2009).
41. J. V. Gerasimenko, Y. Maruyama, K. Yano, N. J. Dolman, A. V. Tepikin, O. H. Petersen, O. V. Gerasimenko, NAADP mobilizes Ca2+ from a thapsigargin-sensitive store in the nuclear envelope by activating ryanodine receptors. *J. Cell Biol.* **163**, 271-282 (2003).
42. T. Rahman, X. Cai, G. C. Brailoiu, M. E. Abood, E. Brailoiu, S. Patel, Two-pore channels provide insight into the evolution of voltage-gated Ca^{2+} and Na^{+} channels. *Sci Signal* **7**, ra109 (2014).
43. T. Vervliet, J. B. Parys, G. Bultynck, Bcl-2 and FKBP12 bind to IP3 and ryanodine receptors at overlapping sites: the complexity of protein-protein interactions for channel regulation. *Biochem. Soc. Trans.* **43**, 396-404 (2015).
44. C. Eroglu, N. J. Allen, M. W. Susman, N. A. O'Rourke, C. Y. Park, E. Ozkan, C. Chakraborty, S. B. Mulinyawe, D. S. Annis, A. D. Huberman, E. M. Green, J. Lawler, R. Dolmetsch, K. C. Garcia, S. J. Smith, Z. D. Luo, A. Rosenthal, D. F. Mosher, B. A. Barres, Gabapentin receptor alpha2delta-1 is a neuronal thrombospondin receptor responsible for excitatory CNS synaptogenesis. *Cell* **139**, 380-392 (2009).
45. G. M. Martin, M. W. Sung, Z. Yang, L. M. Innes, B. Kandasamy, L. L. David, C. Yoshioka, S. L. Shyng, Mechanism of pharmacochaperoning in a mammalian KATP channel revealed by cryo-EM. *eLife* **8**, (2019).
46. E. Aydar, C. P. Palmer, V. A. Klyachko, M. B. Jackson, The sigma receptor as a ligand-regulated auxiliary potassium channel subunit. *Neuron* **34**, 399-410 (2002).
47. H. A. O'Malley, L. L. Isom, Sodium channel beta subunits: emerging targets in channelopathies. *Annu. Rev. Physiol.* **77**, 481-504 (2015).
48. C. J. Penny, B. S. Kilpatrick, E. R. Eden, S. Patel, Coupling acidic organelles with the ER through Ca(2)(+) microdomains at membrane contact sites. *Cell Calcium* **58**, 387-396 (2015).
49. L. Li, T. T. Zeng, B. Z. Zhang, Y. Li, Y. H. Zhu, X. Y. Guan, Overexpression of HN1L promotes cell malignant proliferation in non-small cell lung cancer. *Cancer Biol Ther* **18**, 904-915 (2017).
50. L. Li, Y. L. Zheng, C. Jiang, S. Fang, T. T. Zeng, Y. H. Zhu, Y. Li, D. Xie, X. Y. Guan, HN1L-mediated transcriptional axis AP-2gamma/METTL13/TCF3-ZEB1 drives tumor growth and metastasis in hepatocellular carcinoma. *Cell Death Differ.* **26**, 2268-2283 (2019).
51. Y. Liu, D. S. Choi, J. Sheng, J. E. Ensor, D. H. Liang, C. Rodriguez-Aguayo, A. Polley, S. Benz, O. Elemento, A. Verma, Y. Cong, H. Wong, W. Qian, Z. Li, S. Granados-Principal, G. Lopez-Berestein, M. D. Landis, R. R. Rosato, B. Dave, S. Wong, D. Marchetti, A. K. Sood, J. C. Chang, HN1L Promotes Triple-Negative Breast Cancer Stem Cells through LEPR-STAT3 Pathway. *Stem Cell Reports* **10**, 212-227 (2018).
52. J. Petroziello, A. Yamane, L. Westendorf, M. Thompson, C. McDonagh, C. Cerveny, C. L. Law, A. Wahl, P. Carter, Suppression subtractive hybridization and expression profiling identifies a unique set of genes overexpressed in non-small-cell lung cancer. *Oncogene* **23**, 7734-7745 (2004).
53. C. Grimm, K. Bartel, A. M. Vollmar, M. Biel, Endolysosomal Cation Channels and Cancer-A Link with Great Potential. *Pharmaceuticals (Basel)* **11**, 10.3390/ph11010004 (2018).

54. P. Faris, M. Shekha, D. Montagna, G. Guerra, F. Moccia, Endolysosomal Ca(2+) Signalling and Cancer Hallmarks: Two-Pore Channels on the Move, TRPML1 Lags Behind! *Cancers (Basel)* **11**, 27 (2018).
55. G. P. Johnston, B. Bradel-Tretheway, P. D. Piehowski, H. M. Brewer, B. N. R. Lee, N. T. Usher, J. L. R. Zamora, V. Ortega, E. M. Contreras, J. R. Teuton, J. P. Wendler, K. M. Matz, J. N. Adkins, H. C. Aguilar, Nipah Virus-Like Particle Egress Is Modulated by Cytoskeletal and Vesicular Trafficking Pathways: a Validated Particle Proteomics Analysis. *mSystems* **4**, 10.1128/mSystems.00194-00119 (2019).
56. K. K. F. Ohgane, K. Dodo, Y. Hashimoto, Discovery of oxysterol-derived pharmacological chaperones for NPC1: implication for the existence of second sterol-binding site. *Chem & Biol* **20**, S18-20 (2013).
57. M. Postaa, V. Soosb, P. Beiera, Design of photoaffinity labeling probes derived from 3,4,5-trimethylfuran-2(5H)-one for mode of action elucidation. *Tetrahedron* **72**, 3809-3917 (2016).
58. C. J. Trabbic, F. Zhang, T. F. Walseth, J. T. Slama, Nicotinic Acid Adenine Dinucleotide Phosphate Analogues Substituted on the Nicotinic Acid and Adenine Ribosides. Effects on ReceptorMediated Ca(2)(+) Release. *J. Med. Chem.* **58**, 3593-3610 (2015).
59. B. Zybailov, A. L. Mosley, M. E. Sardiu, M. K. Coleman, L. Florens, M. P. Washburn, Statistical analysis of membrane proteome expression changes in Saccharomyces cerevisiae. *Journal of proteome research* **5**, 2339-2347 (2006).
60. Y. Yang, L. Du, C. Liu, L. Wang, C. Ma, J. Tang, R. S. Baric, S. Jiang, F. Li, Receptor usage and cell entry of bat coronavirus HKU4 provide insight into bat-to-human transmission of MERS coronavirus. *Proc. Natl. Acad. Sci. U. S. A.* **111**, 12516-12521 (2014).
61. R. Aarhus, R. M. Graeff, D. M. Dickey, T. F. Walseth, H. C. Lee, ADP-ribosyl cyclase and CD38 catalyze the synthesis of a calcium-mobilizing metabolite from NADP. *J. Biol. Chem.* **270**, 30327-30333 (1995).

Acknowledgements: All authors would like to thank TFW on his retirement for his support and encouragement of this project over the last decade. Funding: Work was supported by NIH GM088790 (GSG, to JSM), and NSF 2027748 R15-GM131329 (SH, to JTS and TFW) and P30 DA 013429 (EB, to EMU). SP was supported by BBSRC grants (BB/N01524X/1; BB/T015853/1).
Author contributions: GSG, TFW, EB and EMU performed experiments or analyzed data. SH and JTS performed chemical synthesis and validation. SP performed bioinformatic and phylogenetic analyses. GSG directed the project with help from JTS, TFW and JSM. GSG and JSM co-wrote the manuscript with help from other authors. **Competing interests:** The authors declare that they have no competing interests. **Data and materials availability:** All data needed to evaluate the conclusions in this study are present within the paper or the Supplementary Materials.

Figure Legends

Fig. 1. Characterization of NAADP-BP in human erythrocytes. (**A** and **B**), Red Blood Cell (RBC), Jurkat, and U2OS whole cell lysates (WCL) were photolabeled with [^{32}P]-alkyne-AIOC-NAADP (3nM) in the absence or presence of competing unlabeled NAADP (10µM). (**C** and **D**), RBC WCL, S20 cytosol fraction, and "ghost" membrane preparations were photolabeled with [^{32}P]-alkyne-AIOC-NAADP (3nM) in the absence or presence of competing unlabeled NAADP (10µM). (**E** and **F**) RBC S20 was photolabeled with [^{32}P]-alkyne-AIOC-NAADP (3nM) in the presence of the indicated compounds (10µM). (**G** and **H**) RBC S20 was photolabeled with [^{32}P]-alkyne-AIOC-NAADP (3nM) in the presence of either NAADP or NADP at the indicated concentration. Data in (B, D, F, H) represent mean ± SD from densitometry analyses of *n* = 3 independent experiments, where representative gels for each specific assay (A, C, E and G) are shown. 30µg of protein was used for all labeling reactions. Data are shown as mean ± SEM. Statistical significance was assessed using a univariate regression model (see Methods, * P<0.05, ** P<0.01, *** P<0.005). A.U., arbitrary units.

Fig. 2. Biochemical enrichment and isolation of NAADP-BP. (**A**) Schematic representation of NAADP-BP enrichment. Red blood cell S20 proteins were sequentially fractionated in a series of chromatography steps: *i*. strong anion exchange (SAX) at pH 8.5, *ii*. Strong cation exchange (SCX) at pH 7.0, *iii.* hydrophobic interaction chromatography (HIC), *iv.* immobilized metal affinity chromatography (IMAC). Eluates from a phosphoprotein enrichment resin were then photoaffinity labeled, and fall-through was collected after passing protein through phosphoprotein enrichment resin a 2nd time (*v-vii)*. t. (**B**) Structure of alkyne-AIOC-NAADP, photolabile aryl azide (*) and 'clickable' alkyne (**) moieties are shown. (**C**) silver stain *(left)* and phosphorimage *(right)* of 10µg of sample enriched with NAADP-BP. (**D**) depiction of approach, NAADP-BP is crosslinked to the "clickable" alkyne-AIOC-NAADP photoprobe, which is biotinylated by copper-catalyzed azide-alkyne cycloaddition (CuAAC). Biotinylated protein is isolated using neutravidin agarose beads. (**E**) probe-bound NAADP-BP was used in "click" chemistry reaction in absence or presence of biotin-azide-Plus. Biotinylated protein was captured with neutravidin agarose beads, stringently washed, and eluted. Silver stain *(left)* and phosphorimage *(right)* of eluates. Bands of interest are highlighted (blue box). (**F**) Gel bands of isolated NAADP-BP and corresponding bands from input samples and unbiotinylated controls were analyzed by mass spectrometry. Normalized spectral abundance factor (NSAF) after click and capture minus NSAF of unbiotinylated control samples is shown. (**G**) Western blot detection of JPT2 in erythrocyte S20 supernatant after fractionation by anion exchange (ANX), cation exchange (CAX), hydrophobic interaction chromatography (HIC), immobilized metal affinity chromatography (IMAC), or sequential fractionation through each of these steps (serial).

Fig. 3. JPT2 expression analyses. (**A**) mRNA expression profiling in 64 human cell lines ordered from high to low abundance for JPT2 (black), TPC1 (orange) and TPC2 (blue), with SKBR3 and U2OS cells highlighted (yellow). Data and Image credit to the Human protein atlas (17): ENSG00000206053-JPT2/cell, available from v19.proteinatlas.org. a.u., arbitrary units. Inset, schematic of JPT2 structure to highlight basic residues (white), four repeat motifs (blue) and the

'MASNIF' motif. (**B**) Phylogenomic profile of JPT genes. Schematic depicting the number of JPT and TPC homologues in major animal phyla. Organisms, from left to right (accession numbers for JPT): *Homo sapiens* (NP_653171.1 and NP_001002032.1), *Ciona intestinalis* (XP_009861954.1), *Branchiostoma floridae* (XP_002611678.1), *Strongylocentrotus purpuratus* (XP_011684190.1), *Asterias rubens* (XP_033631490.1), *Centruroides sculpturatus* (XP_023222178.1), *Drosophila melanogaster* (Q9I7K0), *Caenorhabditis elegans*, *Aplysia californica* (XP_005102887.1), *Capitella teleta (*ELU08900.1)*, Schistosoma haematobium.*

Fig. 4. Photolabeling of NAADP-BP following immunoprecipitation or knockdown of JPT2. (**A** and **C**) knockdown of *JPT2* using two non-targeting control siRNAs and two discrete *JPT2*-specific siRNAs in both HEK293 cells (A) and U2OS cells (C). Lysates were photolabeled with [^{32}P]-alkyne-AIOC-NAADP (7nM). (**B** and **D**) densitometry analysis of samples from *n* = 3 independent knockdown experiments. (**E** and **G**) JPT2 was immunoprecipitated from RBC S20 (E) and U2OS S200 (G) using control IgG or two discrete JPT2-specific antibodies. Protein-G beads were used to isolate antibody-protein complexes. *Left*, 10µg of input samples and cleared supernatants after immunoprecipitation were photolabeled with [^{32}P]-alkyne-AIOC-NAADP (7nM). *Right*, immunoprecipitated protein was washed and gently eluted. Eluates were photolabeled with [^{32}P]-alkyne-AIOC-NAADP (7nM). (**F** and **H**) densitometry analysis of photolabeling of immunoprecipitated protein from three independent experiments. Data in (B, D, F, H) are collected from *n* = 3 independent experiments and shown as mean ± SEM. Statistical significance was assessed using a univariate regression model (see Methods, * $P<0.05$, ** $P<0.01$, *** $P<0.005$).

Fig. 5. Recombinant JPT2 binds NAADP. Recombinant JPT2 was incubated with [^{32}P]-NAADP in the presence of increasing concentrations of cold NAADP or NADP. (**A**) Representative phosphorimage of multi-well plates used in binding experiments. (**B**) Quantification of bound [^{32}P]-NAADP in the presence of various concentrations of NAADP (closed circle) or NADP (open circle). Data represents mean densitometry [^{32}P] values ± SD from *n* = 3 independent experiments.

Fig. 6. JPT2 interacts with TPC1 to regulate NAADP-evoked Ca^{2+} release. (**A**) Co-immunoprecipitation of JPT2 with TPC1. *Left,* input controls of lysates from HEK293 cells overexpressing TPC1-GFP or TPC2-GFP. *Middle*, immunoprecipitation of endogenous JPT2 results in detection of TPC1-GFP. *Right*, immunoprecipitation of TPC1-GFP results in detection of endogenous JPT2. Data show representative gels from *n* = 3 independent transfections. (**B**) Traces of intracellular Ca^{2+} flux in response to microinjection of buffer (black) or NAADP (blue, 10µM pipette concentration) in individual U2OS cells treated with two different non-targeting control siRNAs (ctrl siRNA #1 & #2, green) or JPT2-specific siRNAs (siRNA #1 & #2, red). Individual single cell responses are shown, with the averaged trace bolded. (**C**) Averaged peak amplitude ± SD (*left*) and average area under the curve (AUC, *right*) is shown from $n \geq 5$ independent cellular injections. *P*-values versus NAADP injections in untransfected control cells. Data are shown as mean ± SEM, * $P<0.05$, ** $P<0.01$, *** $P<0.005$.

Fig. 7. JPT2 regulates SARS-CoV-2 translocation through the endolysosomal system. (**A**) Schematic to show different routes of SARS-CoV-2 cell entry mediated by ACE2 internalization and translocation through acidic Ca^{2+} stores (left) or fusion at the plasma membrane following spike protein activation by TMPRSS2 (right). (**B**) Data report luciferase activity in cell lysates after transduction with a luciferase-encoding SARS-CoV-2 pseudovirus. HEK293 cells expressing ACE2 were transduced with SARS-CoV-2 pseudovirus in the presence of the indicated compound (10μM). Drugs represent known inhibitors of IP_3Rs (2-APB, xestospongin), RyRs (dantrolene, ryanodine), and inhibitors of NAADP-evoked Ca^{2+} release (tetrandrine, PF-543, SKF96365, racecadotril, salmeterol). (**C**) Identical drug treatments in HEK293 cells overexpressing TMPRSS2. (**D** and **E**) Assays performed in HEK293 cells after transfection with the indicated siRNAs. Cells are transfected with plasmid encoding (D) ACE2 or (E) TMPRSS2, except where indicated (untransfected). Data represent results from $n = 3$ independent assays, with values shown as mean ± SEM. Statistical significance was assessed using a univariate regression model (see Methods, * $P<0.05$, ** $P<0.01$, *** $P<0.005$).

Table 1

	Identified Protein		*MW (kDa)*	Input		*Negative Control*		Dde-biotin click		*Negative Control*		Plus-biotin click	
				1	2	1	2	1	2	3	4	3	4
1	Jupiter microtubule associated homolog 2	JPT2	20	3	7	0	0	231	234	0	0	40	23
2	Hemoglobin subunit alpha	HBA1	15	10	12	11	7	47	61	6	10	30	14
3	Hemoglobin subunit beta	HBB	16	10	16	6	3	35	41	5	15	26	18
4	Hemoglobin subunit delta	HBD	16	6	14	5	0	30	32	4	11	21	14
5	Junction plakoglobin	JUP	82	8	33	17	7	6	2	14	16	32	0
6	Flavin reductase (NADPH)	BLVRB	22	12	5	0	0	30	9	0	7	24	11
7	Peroxiredoxin-2	PRDX2	22	18	7	3	0	16	8	3	6	10	7
8	Ubiquitin-40S ribosomal protein S27a	RPS27a	18	19	5	0	0	18	4	3	7	9	3
9	Desmoglein-1	DSG1	114	2	13	5	4	0	0	8	9	20	4
10	Filaggrin-2	FLG2	248	7	11	2	0	5	0	8	7	25	0
11	L-xylulose reductase	DCXR	26	16	8	0	0	21	8	0	0	7	0
12	Glyceraldehyde-3-phosphate dehydrogenase	GAPDH	36	5	5	4	0	17	6	3	2	6	2
13	Actin, cytoplasmic 1	ACTB	42	4	2	0	8	5	0	7	7	12	0
14	Peroxiredoxin-1	PRDX1	22	7	5	0	0	10	0	0	0	11	6
15	Serum albumin precursor Isoform 1	ALB	69	6	0	5	4	0	0	7	8	9	0
16	Carbonic anhydrase 1	CA1	29	3	0	2	0	12	4	0	0	6	3
17	Hemoglobin subunit gamma-2	HBG2	16	4	0	0	0	18	0	0	0	6	0
18	Annexin A2	ANXA2	39	2	5	4	2	0	0	3	3	9	0
19	Carbonic anhydrase 2	CA2	29	0	0	3	0	14	4	0	0	5	2
20	Desmocollin-1	DSC1	100	0	3	6	0	0	0	2	5	8	0

Table 1. Mass spectrometry dataset. Table depicts total number of spectral counts (*59*) associated with each identified protein in the indicated experimental samples. First two columns represent samples prior to treatment with click chemistry reagents ('input') and without neutravidin-agarose pulldown. The next four columns represent samples treated with click reagents either in the absence ('negative control') or presence of Dde-biotin-picolyl-azide ('Dde-biotin') prior to neutravidin agarose pulldown. The final four columns depict samples treated with click reagents either in the absence ('negative control') or presence of biotin-azide-Plus ('Plus-biotin') prior to neutravidin agarose pulldown. Table is ranked by total spectral count as the top twenty hits.

Figure 1

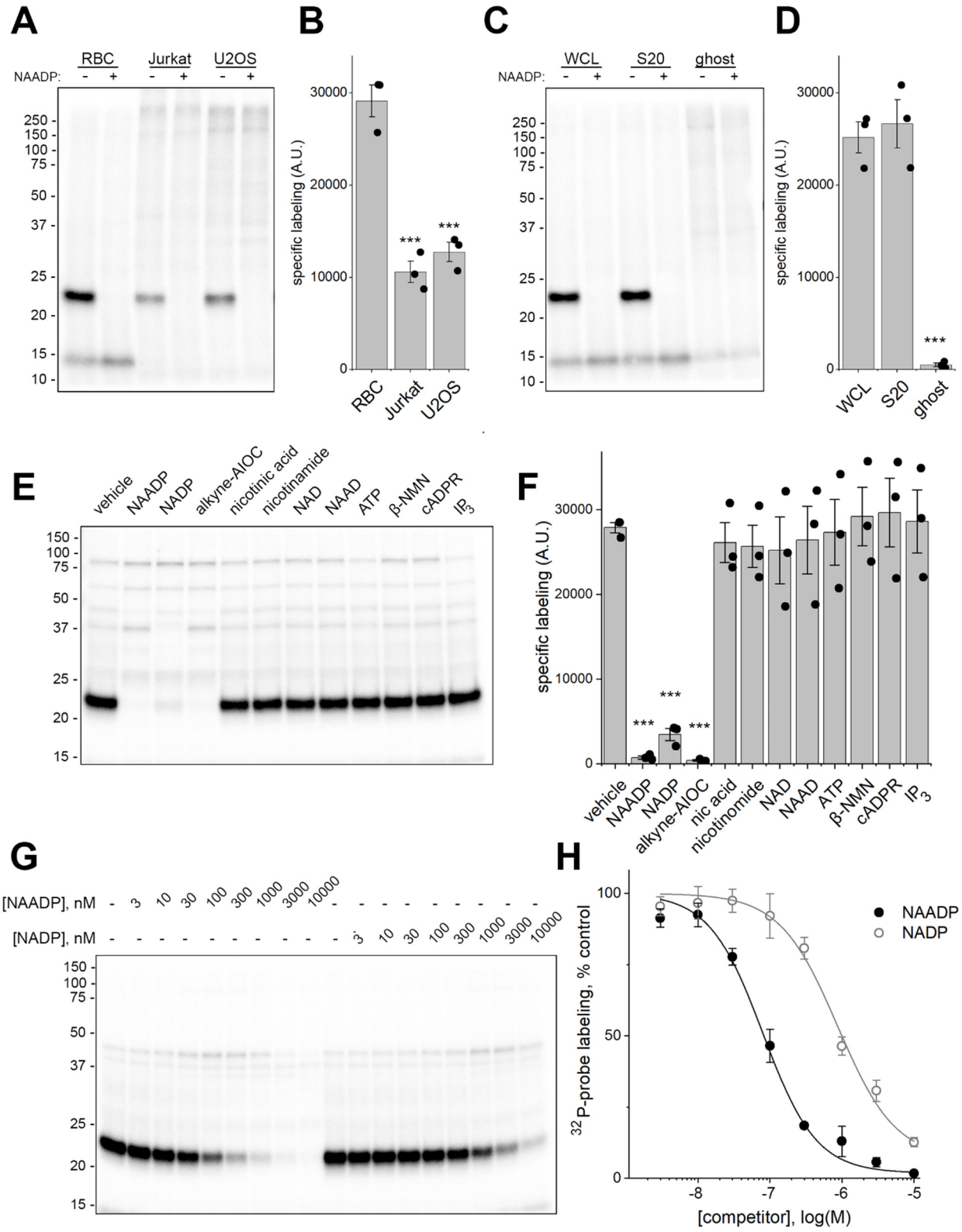
A
RBC
Jurkat
U2OS
NAADP: - + - + - +
250
150
100
75
50
37
25
20
15
10
B
specific labeling (A.U.)
30000
20000
10000
0
***
***
RBC
Jurkat
U2OS
C
WCL
S20
ghost
NAADP: - + - + - +
D
WCL
S20
ghost
E
vehicle
NAADP
NADP
alkyne-AIOC
nicotinic acid
nicotinamide
NAD
NAAD
ATP
β-NMN
cADPR
IP3
F
vehicle
NAADP
NADP
alkyne-AIOC
nic acid
nicotinomide
NAD
NAAD
ATP
β-NMN
cADPR
IP3
G
[NAADP], nM - 3 10 30 100 300 1000 3000 10000 - - - - - - - -
[NADP], nM - - - - - - - - - 3 10 30 100 300 1000 3000 10000
H
NAADP
NADP
32P-probe labeling, % control
[competitor], log(M)

Figure 2

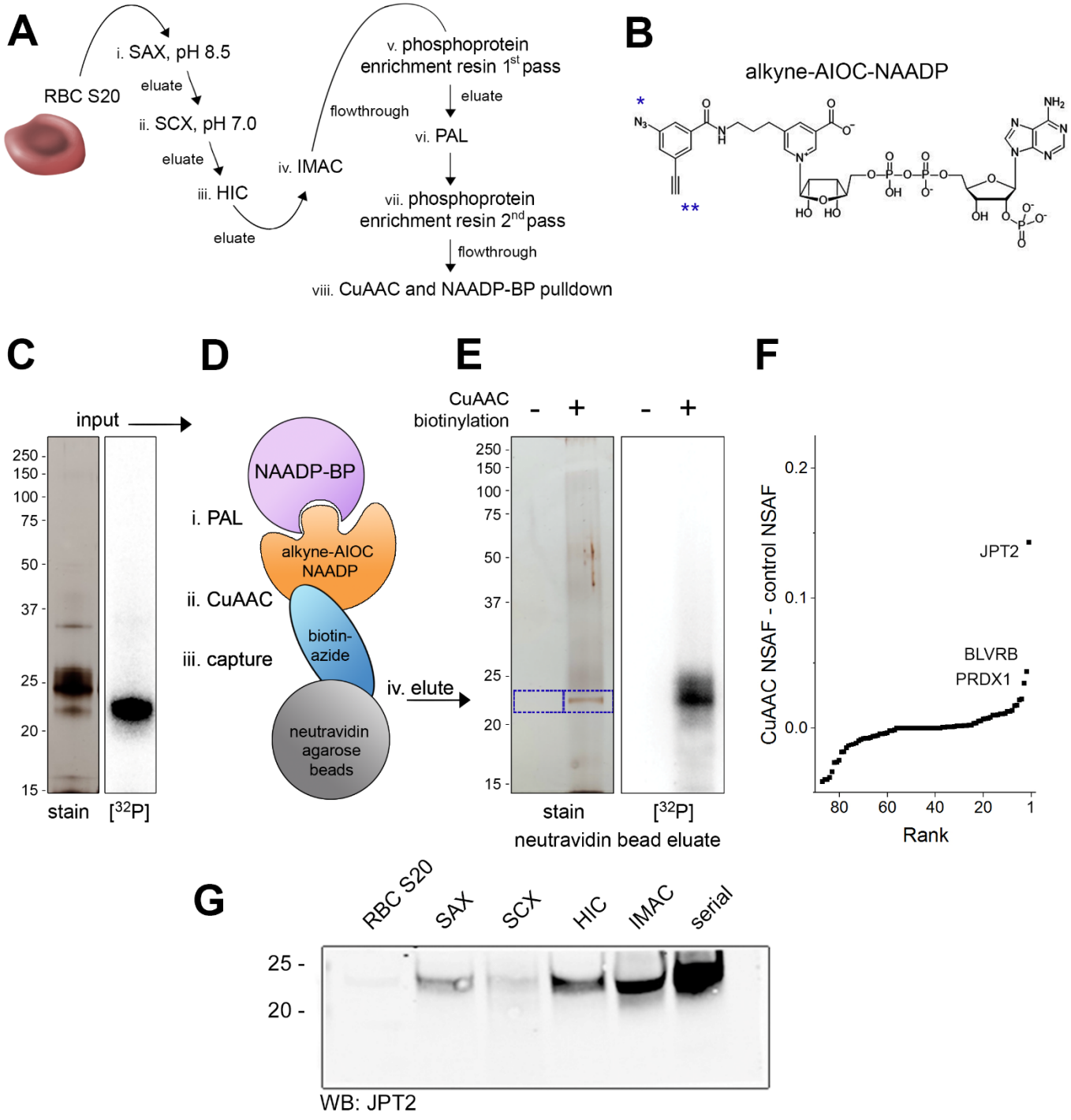
A
RBC S20
i. SAX, pH 8.5
eluate
ii. SCX, pH 7.0
eluate
iii. HIC
eluate
iv. IMAC
flowthrough
v. phosphoprotein enrichment resin 1st pass
eluate
vi. PAL
vii. phosphoprotein enrichment resin 2nd pass
flowthrough
viii. CuAAC and NAADP-BP pulldown
B
alkyne-AIOC-NAADP
C
input
250
150
100
75
50
37
25
20
15
stain
[32P]
D
NAADP-BP
i. PAL
alkyne-AIOC NAADP
ii. CuAAC
biotin-azide
iii. capture
neutravidin agarose beads
iv. elute
E
CuAAC biotinylation
- + - +
250
150
100
75
50
37
25
20
15
stain
[32P]
neutravidin bead eluate
F
CuAAC NSAF - control NSAF
0.2
0.1
0.0
JPT2
BLVRB
PRDX1
80
60
40
20
1
Rank
G
RBC S20
SAX
SCX
HIC
IMAC
serial
25 -
20 -
WB: JPT2

Figure 3

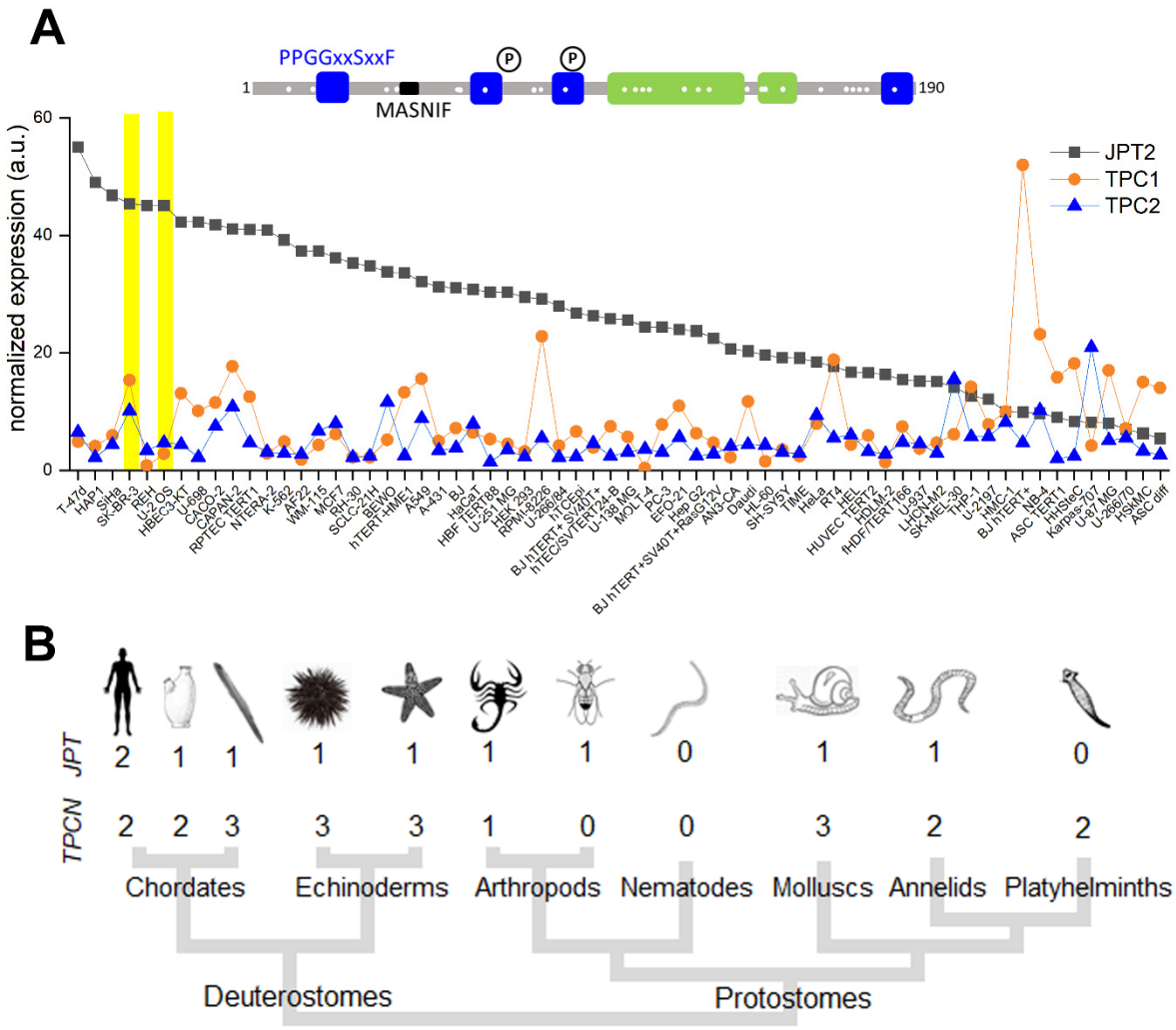
A
PPGGxxSxxF
MASNIF
1
190
normalized expression (a.u.)
60
40
20
0
JPT2
TPC1
TPC2
B
JPT
TPCN
2 1 1 1 1 1 1 0 1 1 0
2 2 3 3 3 1 0 0 3 2 2
Chordates
Echinoderms
Arthropods
Nematodes
Molluscs
Annelids
Platyhelminths
Deuterostomes
Protostomes

Figure 4

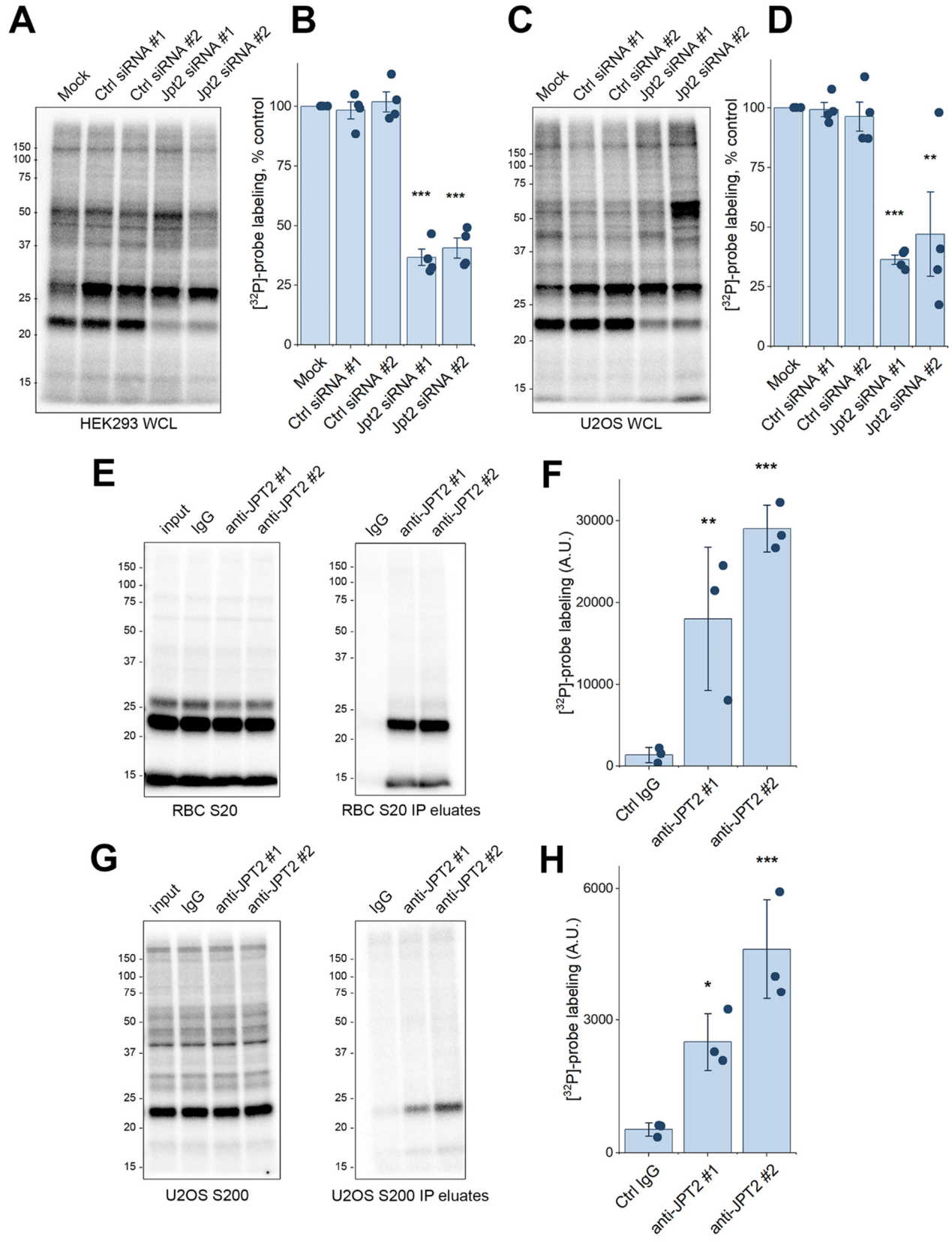
A
Mock
Ctrl siRNA #1
Ctrl siRNA #2
Jpt2 siRNA #1
Jpt2 siRNA #2
150
100
75
50
37
25
20
15
HEK293 WCL
B
[32P]-probe labeling, % control
100
75
50
25
0
***
***
Mock
Ctrl siRNA #1
Ctrl siRNA #2
Jpt2 siRNA #1
Jpt2 siRNA #2
C
Mock
Ctrl siRNA #1
Ctrl siRNA #2
Jpt2 siRNA #1
Jpt2 siRNA #2
150
100
75
50
37
25
20
15
U2OS WCL
D
[32P]-probe labeling, % control
100
75
50
25
0
***
**
Mock
Ctrl siRNA #1
Ctrl siRNA #2
Jpt2 siRNA #1
Jpt2 siRNA #2
E
input
IgG
anti-JPT2 #1
anti-JPT2 #2
150
100
75
50
37
25
20
15
RBC S20
IgG
anti-JPT2 #1
anti-JPT2 #2
150
100
75
50
37
25
20
15
RBC S20 IP eluates
F
[32P]-probe labeling (A.U.)
30000
20000
10000
0
**
***
Ctrl IgG
anti-JPT2 #1
anti-JPT2 #2
G
input
IgG
anti-JPT2 #1
anti-JPT2 #2
150
100
75
50
37
25
20
15
U2OS S200
IgG
anti-JPT2 #1
anti-JPT2 #2
150
100
75
50
37
25
20
15
U2OS S200 IP eluates
H
[32P]-probe labeling (A.U.)
6000
3000
0
*
***
Ctrl IgG
anti-JPT2 #1
anti-JPT2 #2

Figure 5

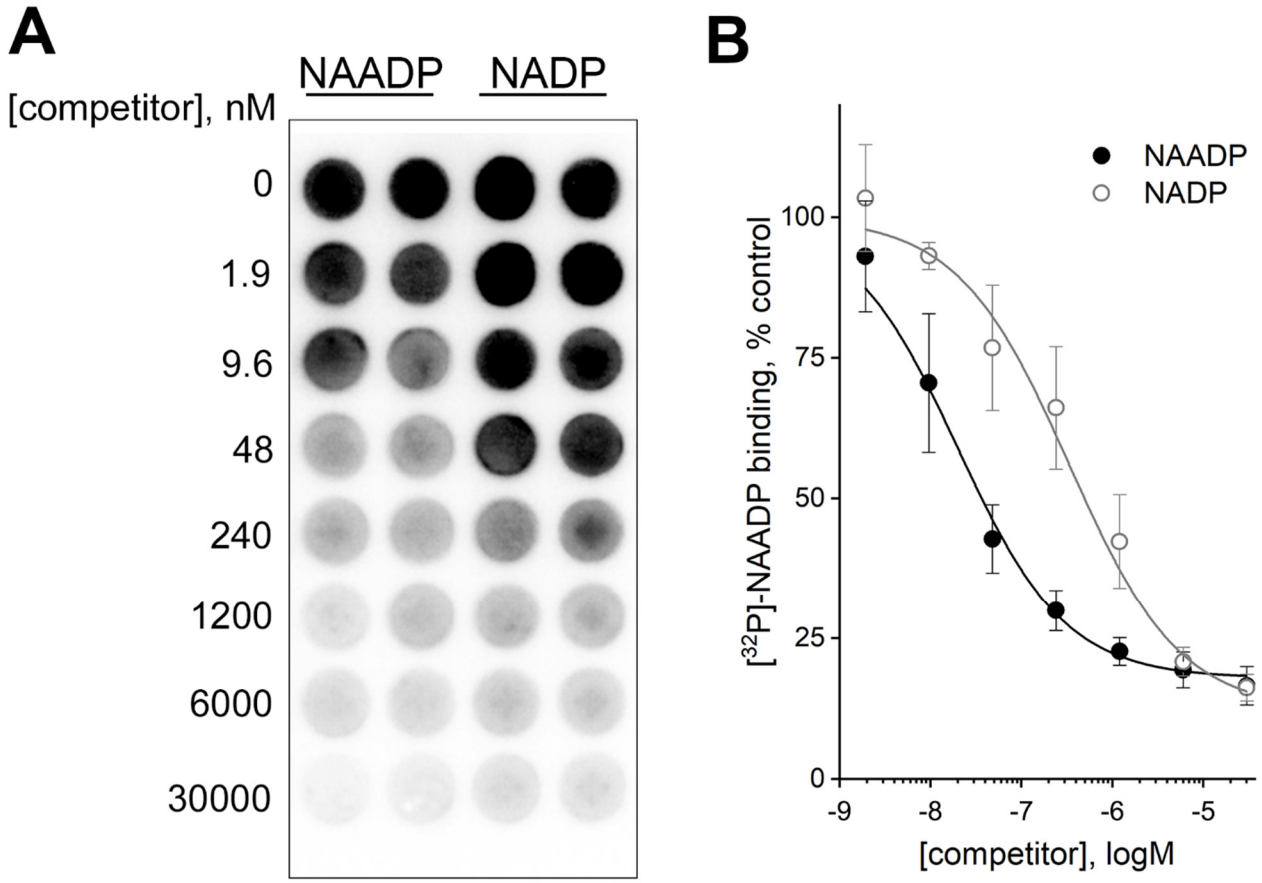
A
NAADP
NADP
[competitor], nM
0
1.9
9.6
48
240
1200
6000
30000
B
NAADP
NADP
[32P]-NAADP binding, % control
100
75
50
25
0
-9
-8
-7
-6
-5
[competitor], logM

Figure 6

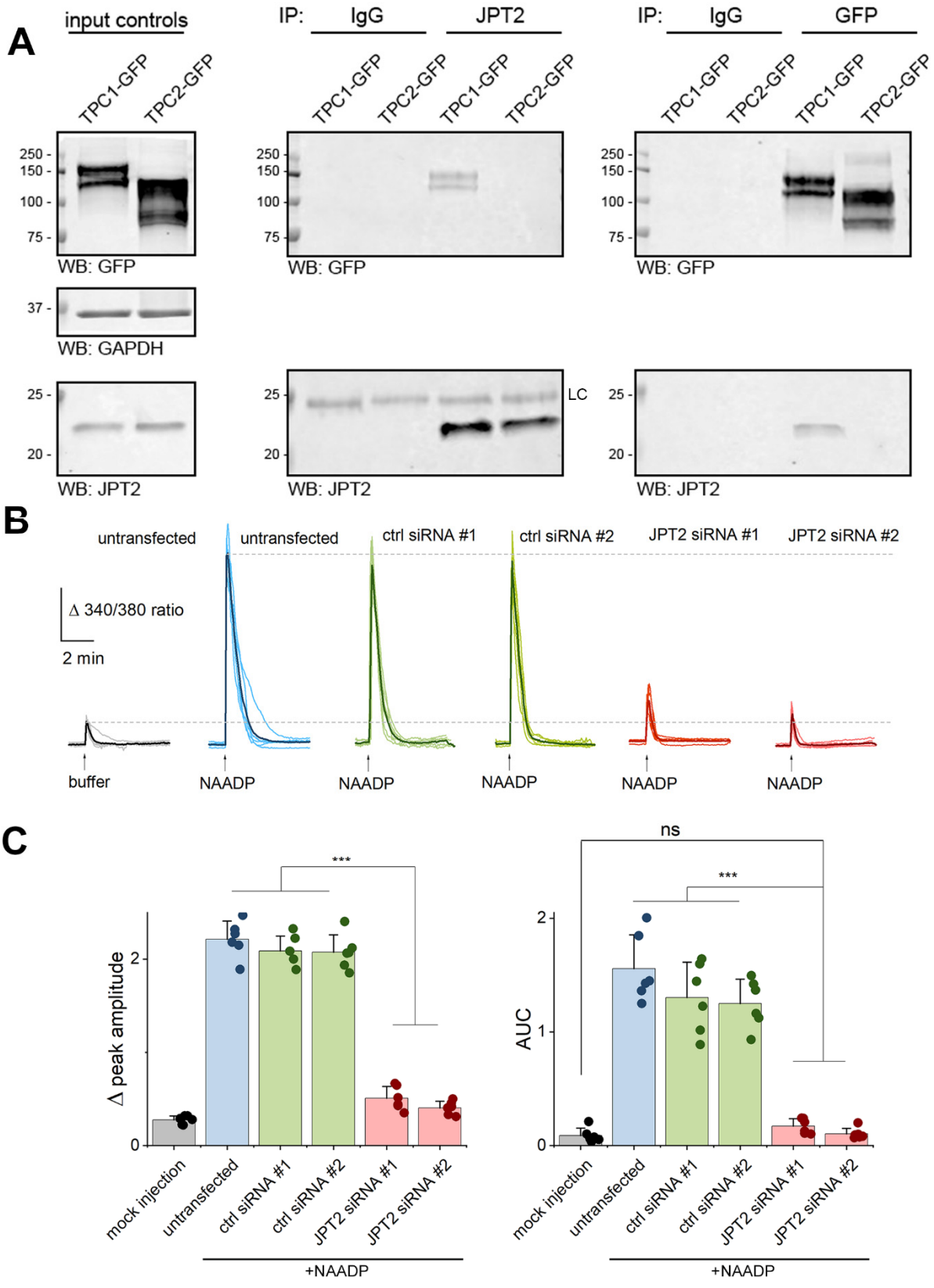
A
input controls
IP: IgG JPT2
IP: IgG GFP
TPC1-GFP
TPC2-GFP
250
150
100
75
WB: GFP
37
WB: GAPDH
25
20
WB: JPT2
LC
B
untransfected
untransfected
ctrl siRNA #1
ctrl siRNA #2
JPT2 siRNA #1
JPT2 siRNA #2
Δ 340/380 ratio
2 min
buffer
NAADP
C
Δ peak amplitude
AUC
ns
***
mock injection
untransfected
ctrl siRNA #1
ctrl siRNA #2
JPT2 siRNA #1
JPT2 siRNA #2
+NAADP

Figure 7

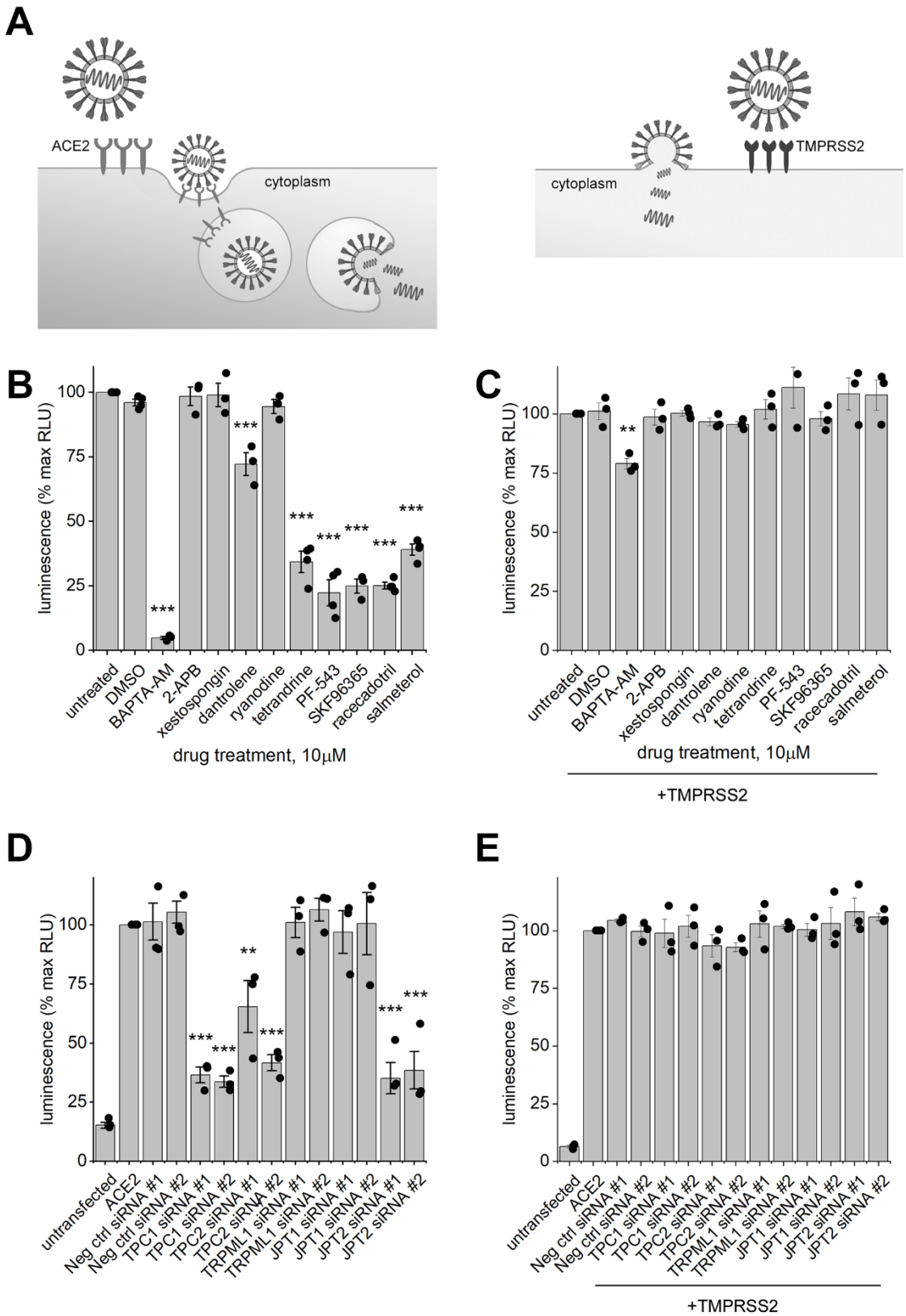
A
ACE2
cytoplasm
TMPRSS2
cytoplasm
B
luminescence (% max RLU)
untreated
DMSO
BAPTA-AM
2-APB
xestospongin
dantrolene
ryanodine
tetrandrine
PF-543
SKF96365
racecadotril
salmeterol
drug treatment, 10μM
C
luminescence (% max RLU)
drug treatment, 10μM
+TMPRSS2
D
luminescence (% max RLU)
untransfected
ACE2
Neg ctrl siRNA #1
Neg ctrl siRNA #2
TPC1 siRNA #1
TPC1 siRNA #2
TPC2 siRNA #1
TPC2 siRNA #2
TRPML1 siRNA #1
TRPML1 siRNA #2
JPT1 siRNA #1
JPT1 siRNA #2
JPT2 siRNA #1
JPT2 siRNA #2
E
luminescence (% max RLU)
+TMPRSS2

Supplementary Materials

Supplementary Figure S1. Chromatographic enrichment of NAADP-BP.

Supplementary Figure S2. Validation of knockdown.

Supplementary Figure 1

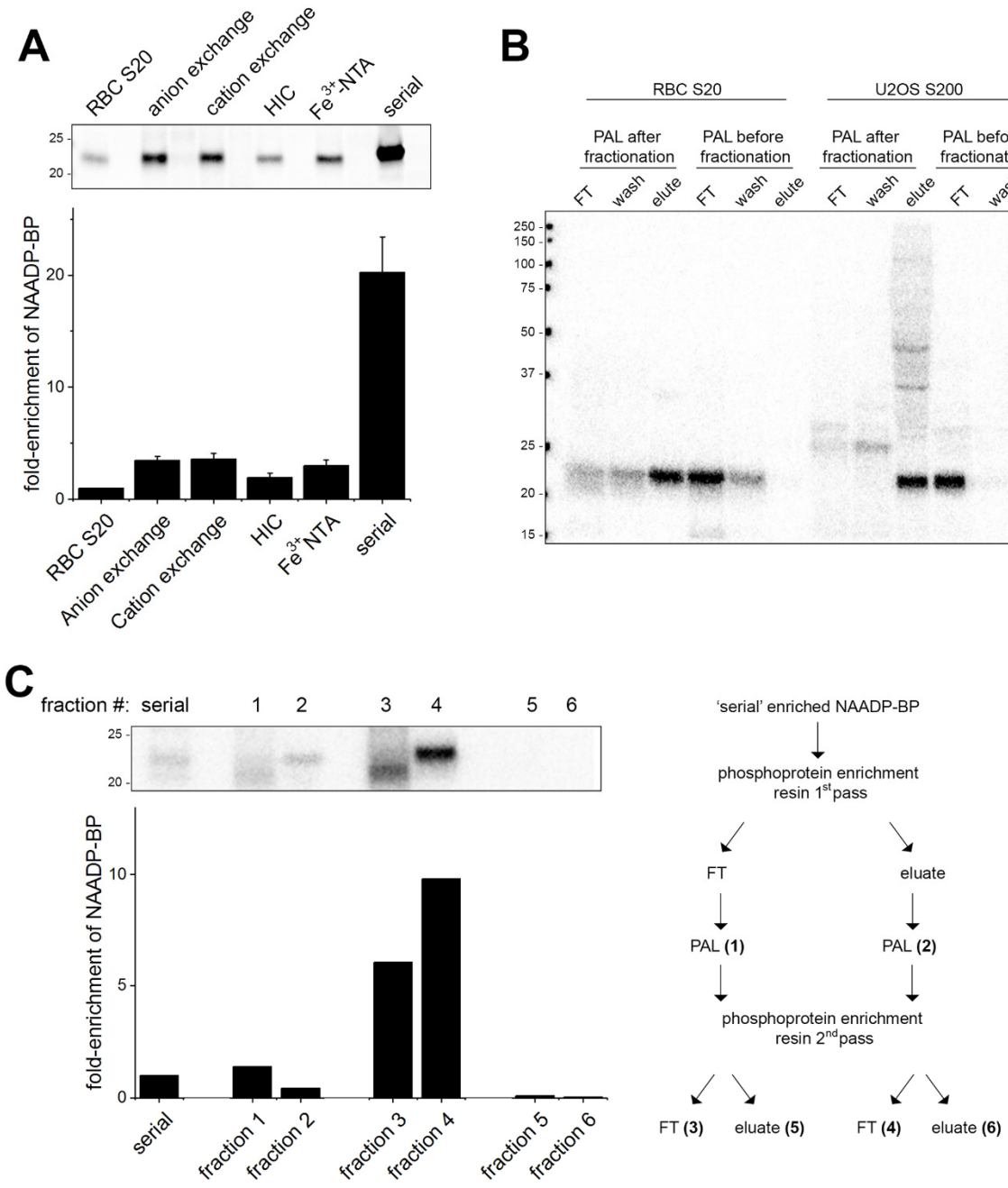

Supplementary Figure 1. Chromatographic enrichment of NAADP-BP. A, RBC S20 was fractionated using a variety of chromatography resins. 5µg of protein eluted from the indicated resin, or from sequential fractionation of all resins (serial), was photolabeled with [^{32}P]-alkyne-AIOC-NAADP (5nM) in the absence or presence of competing unlabeled NAADP (10µM). *Top*, representative phosphorimage. *Bottom,* densitometry analysis. **B,** RBC S20 or U2OS S200 lysates were fractionated using a phosphoprotein enrichment resin using a batch-binding method, flowthrough (FT), washes, and eluates are shown. Samples were photolabeled with [^{32}P]-alkyne-AIOC-NAADP (5nM) either before or after fractionation. After treatment, 2µg of samples from RBC S20 or 30µg of samples from U2OS S200 were separated by SDS-PAGE. **C**, protein sample from (A) was fractionated using a phosphoprotein enrichment resin. Flowthrough and eluates were photolabeled with alkyne-AIOC-NAADP (1µM, 90% of sample) or with [^{32}P]-alkyne-AIOC-NAADP (5nM, 10% of sample), labeling reactions were mixed after UV-induced crosslinking. After photolabeling, flowthrough and eluate samples were independently fractionated over phosphoprotein enrichment resin again. *Top*, representative phosphorimage of 2µg of protein for each condition. *Bottom,* densitometry analyses. *Right*, schematic of phosphoprotein enrichment resin fractionation.

Supplementary Figure 2

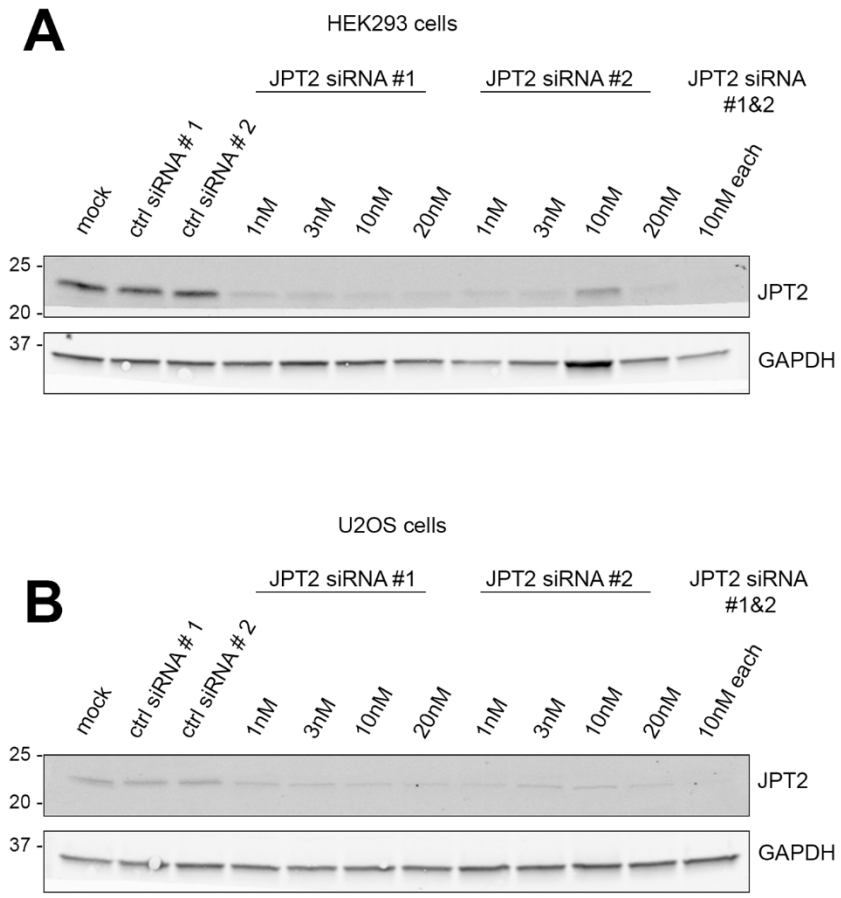

Supplementary Figure 2. Validation of knockdown. HEK293 cells and U2OS cells were transfected with dual non-targeting control siRNAs (20nM) or dual JPT2-specific siRNAs at the indicated concentrations or treated with transfection reagent alone (mock). Lysates from HEK293 cells (**A**) and U2OS cells (**B**) were immunoblotted for endogenous JPT2 (top) or GAPDH (bottom). Representative blots are shown for each condition.